

AD-A261 965



12

AD

AD-E402 397

Special Publication ARAED-SP-92003

**THERMAL DECOMPOSITION OF ENERGETIC MATERIALS.
3. TEMPORAL BEHAVIORS OF THE RATES OF FORMATION OF
THE GASEOUS PYROLYSIS PRODUCTS FROM CONDENSED-
PHASE DECOMPOSITION OF 1,3,5-TRINITROHEXAHYDRO-S-
TRIAZINE**

Richard Behrens, Jr.
Combustion Research Facility
Sandia National Laboratories
Livermore, CA 94551

Suryanarayana Bulusu
ARDEC

DTIC
SELECTE
MAR 12 1993
S B D

February 1993



US ARMY
ARMAMENT RESEARCH
& CHEMICAL COMMAND
ARMAMENT RDE CENTER

**U.S. ARMY ARMAMENT RESEARCH, DEVELOPMENT AND
ENGINEERING CENTER**

Armament Engineering Directorate
Picatinny Arsenal, New Jersey

Approved for public release; distribution is unlimited.

98 3 11 068

93-05238



2304

The views, opinions, and/or findings contained in this report are those of the authors(s) and should not be construed as an official Department of the Army position, policy, or decision, unless so designated by other documentation.

The citation in this report of the names of commercial firms or commercially available products or services does not constitute official endorsement by or approval of the U.S. Government.

Destroy this report when no longer needed by any method that will prevent disclosure of its contents or reconstruction of the document. Do not return to the originator.

REPORT DOCUMENTATION PAGE			Form Approved OMB No. 0704-0188	
Public reporting burden for this collection of information is estimated to average 1 hour per response, including the time for reviewing instructions, searching existing data sources, gathering and maintaining the data needed, and completing and reviewing the collection of information. Send comments regarding this burden estimate or any other aspect of this collection of information, including suggestions for reducing this burden, to Washington Headquarters Services, Directorate for Information Operation and Reports, 1215 Jefferson Davis Highway, Suite 1204, Arlington, VA 22202-4302, and to the Office of Management and Budget, Paperwork Reduction Project (0704-0188), Washington, DC 20503.				
1. AGENCY USE ONLY (Leave blank)	2. REPORT DATE February 1993		3. REPORT TYPE AND DATES COVERED Technical	
4. TITLE AND SUBTITLE Thermal Decomposition of Energetic Materials. 3. Temporal Behavior of the Rates of Formation of the Gaseous Pyrolysis Products from Condensed-Phase Decomposition of 1,3,5-Trinitrohexahydro-s-triazine			5. FUNDING NUMBERS	
6. AUTHOR(S) Richard Behrens, Jr., Sandia National Laboratories Suryanarayana Bulusu, ARDEC				
7. PERFORMING ORGANIZATION NAME(S) AND ADDRESSES(S) Combustion Research Facility ARDEC, AED Sandia National Laboratories Energetics & Warheads Div (SMCAR-AEE) Livermore, CA 94551 Picatinny Arsenal, NJ 07806-5000			8. PERFORMING ORGANIZATION REPORT NUMBER Special Publication ARAED-SP-92003	
9. SPONSORING/MONITORING AGENCY NAME(S) AND ADDRESS(S) ARDEC, IMD STINFO Br (SMCAR-IMI-I) Picatinny Arsenal, NJ 07806-5000			10. SPONSORING/MONITORING AGENCY REPORT NUMBER	
11. SUPPLEMENTARY NOTES				
12a. DISTRIBUTION/AVAILABILITY STATEMENT Approved for public release; distribution is unlimited.			12b. DISTRIBUTION CODE	
13. ABSTRACT (Maximum 200 words) Through the use of simultaneous thermogravimetry modulated beam mass spectrometry (STMBMS) measurements, time-of-flight (TOF) velocity-spectra analysis, and 2H, 13C, 15N, and 18O labeled analogues of 1,3,5-trinitrohexahydro-s-triazine (RDX), the thermal decomposition products of RDX have been identified as H ₂ O, HCN, CO, CH ₂ O, NO, N ₂ O, NH ₂ CHO, NO ₂ , HONO, (CH ₃)NHCHO, oxy-s-triazine (OST), and 1-nitroso-3,5-dinitrohexahydro-s-triazine (ONDNTA) and all of their gas formation rates have been measured as a function of time. From these results the primary reaction pathways that control the decomposition of RDX in both the solid and liquid phases have been discovered. Four primary reaction pathways control the decomposition of RDX in the liquid phase between 200 and 215°C. Two pathways are first-order reactions solely in RDX. One produces predominantly OST, NO, and H ₂ O and accounts for approximately 30% of the decomposed RDX, and the other produces predominantly N ₂ O and CH ₂ O with smaller amounts of NO ₂ , CO, and NH ₂ CHO and accounts for 10% of the decomposed RDX. The third pathway consists of formation of ONDNTA by reaction between NO and RDX, followed by the decomposition of ONDNTA to predominantly CH ₂ O and N ₂ O. The fourth reaction pathway consists of decomposition of RDX through reaction with a catalyst that is formed from the decomposition products of previously decomposed RDX. ONDNTA is the only product that appears to be formed during the early stages of decomposition of RDX in the solid phase.				
14. SUBJECT TERMS Thermogravimetry, Modulated beam mass spectrometry, Thermal decomposition, RDX, ONDNTA			15. NUMBER OF PAGES 22	
			16. PRICE CODE	
17. SECURITY CLASSIFICATION OF REPORT UNCLASSIFIED	18. SECURITY CLASSIFICATION OF THIS PAGE UNCLASSIFIED	19. SECURITY CLASSIFICATION OF ABSTRACT UNCLASSIFIED	20. LIMITATION OF ABSTRACT SAR	

CONTENTS

	Page
Introduction	1
Experimental Section	2
Instrument Description	2
Identification of Decomposition Products	3
Quantification Procedure	3
Sample Preparation	3
Results	3
Identification of Decomposition Products	3
Rates of Formation of Thermal Decomposition Products	5
Discussion	8
Lower Molecular Weight (Gaseous) Products	8
Large Molecular Weight Products	8
Decomposition Pathways	9
Conclusions	14
References and Notes	14
Distribution List	17

DTIC QUALITY INSPECTED 5

Accession For	
NTIS GRA&I	<input checked="" type="checkbox"/>
DTIC TAB	<input type="checkbox"/>
Unannounced	<input type="checkbox"/>
Justification	
By _____	
Distribution/	
Availability Codes	
Dist	Avail and/or Special
A-1	

TABLES

		Page
1	Experimental Parameters	3
2	Ion Formulas, m/z Values from Isotopically Labeled Analogues, and Pyrolysis Product Molecular Weights and Formulas from the Thermal Decomposition of RDX	4
3	Quantitative Results from the Thermal Decomposition of RDX	9
4	Fraction of RDX Decomposed by Each Reaction Pathway	13

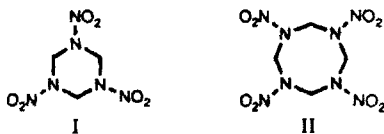
FIGURES

1	Cross section of the reaction cell used for thermal decomposition experiments	3
2	Time-of-flight velocity spectra of ion signals at various m/z values measured with the mass spectrometer	4
3	Time-of-flight velocity spectra of ion signals at various m/z values measured with the mass spectrometer	5
4	Gas formation rates of the thermal decomposition products formed during experiment I using pure unlabeled RDX and a heating rate of 0.58°C/min	6
5	Gas formation rates of the thermal decomposition products formed during experiment II using pure RDX-d ₆ and a heating rate of 0.58°C/min	6
6	Gas formation rates of the thermal decomposition products formed during experiment III using RDX that contains approximately 4% HMX and a heating rate of 0.54°C/min	7

7	Gas formation rate of the ONDNTA formed during experiment IV using pure unlabeled RDX and the release rate of RDX	7
8	Ion signals associated with the thermal decomposition products formed during experiment V using pure unlabeled RDX at an isothermal temperature of 190°C	8
9	Gas formation rates of the products formed in experiment I with unlabeled RDX along with the fits to the data based on the four primary decomposition pathways	10
10	Gas formation rates of the products formed in experiment II with RDX-d ₆ along with the fits to the data based on the four primary decomposition pathways	11

Introduction

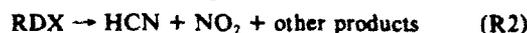
The two similar cyclic nitramines, 1,3,5-trinitrohexahydro-*s*-triazine (RDX, I) and octahydro-1,3,5,7-tetranitro-1,3,5,7-tetrazocine (HMX, II) are energetic ingredients that are used in various propellants and explosives. Understanding the complex



physicochemical processes that underlie the combustion of these materials can lead to methods for modifying the propellant and explosive formulations in which they are used to obtain better ignition, combustion, or sensitivity properties. Since the processes that occur in the condensed phase of these materials ultimately lead to the reactants that are consumed in the gas-phase combustion reactions, it is important to understand these condensed-phase processes. Consequently, our work is aimed at obtaining a better understanding of physical processes and reaction mechanisms that occur in the condensed phase of nitramine compounds so that the identity and rate of release of the pyrolysis products can be predicted, as a function of pressure and heating rate, based on the physical properties and molecular conformation of the materials. The present study examines the thermal decomposition of RDX and compares it to our recent studies on the condensed-phase decomposition of HMX.^{1,2}

Reviews³⁻⁵ of the literature on RDX and HMX have discussed the roles of unimolecular decomposition and autocatalysis on the thermal decomposition of these compounds. The work on RDX has included slow-heating rate thermal decomposition studies,⁶⁻¹⁰ mass spectrometry mass spectrometry studies,¹¹⁻¹⁵ high-heating rate thermal decomposition studies,^{16,17} and studies of shock in-

itiated decomposition.^{18,19} Much of the controversy about the reaction mechanism that controls the decomposition of RDX and HMX centers around the fact that results from these experiments, using different thermal decomposition measurement techniques, have identified different sets of decomposition products. In general, two different sets of products are formed in these experiments

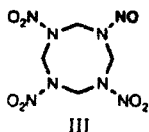


To explain the appearance of these different groups of products, reaction mechanisms based on C-N bond breaking were suggested for N_2O and CH_2O in reaction R1 and N-N bond breaking or four- and five-center HONO elimination reactions for the formation of products in reaction R2. The reasons for why products from reaction R1 were seen in certain types of experiments, whereas products from reaction R2 were seen in other types of experiments, were unclear. Furthermore, simple bond-breaking mechanisms could not explain the apparent "autocatalytic" behavior observed in several thermal decomposition experiments. Arguments, such as the occurrence of a phase change from a solid to a liquid (or molten) state, were put forth to explain the autocatalytic behavior and still allow interpretation of the product identities in terms of unimolecular RDX or HMX bond-breaking sequences. In retrospect, it appears that much of the controversy in interpreting the results of the work carried out by various experimenters stems from the fact that the decompositions of RDX and HMX are complex and consist of several competing reaction pathways that depend on the physical state of the material, as well as its molecular conformation, as it undergoes decomposition. Ultimately, these competing channels produce different thermal decomposition products. Almost all conventional thermal decomposition experiments (i.e., TGA, DTA, DSC, and mass spectrometry analysis) have not been able either to measure the

products larger than those illustrated by reactions R1 and R2 or to monitor the variations in the relative amounts of the products as the chemical composition of the reacting sample changed due to the ongoing decomposition of the initial sample of RDX or HMX.

To circumvent these problems and in an effort to obtain more detailed information on the reaction mechanisms, experiments have been carried out with simpler nitramines, such as dimethylnitramine²⁰⁻²² [(CH₃)₂N-NO₂] (DMNA), which are more amenable to conventional gas-phase decomposition studies. In addition, photodecomposition experiments on RDX²³ under collisionless conditions have provided detailed information on its unimolecular decomposition by using infrared multiphoton dissociation (IRMPD) to fragment RDX molecules in a molecular beam and determine the identity and translational energy of the resulting fragments using mass spectrometry and time-of-flight (TOF) velocity analysis techniques. These two types of experiments have provided valuable insights into how these nitramines decompose. The question that one poses is whether the mechanisms derived from these experiments also control the decomposition of RDX and HMX in the condensed phase. To answer this question, more detailed information is required than has been obtained in the conventional thermal decomposition experiments. Our experiments collect two additional types of data that will aid the understanding of the decomposition of RDX and HMX in the condensed phase. First, important reaction pathways are uncovered by identifying the more complex molecules that may act as intermediates leading to the formation of lower molecular weight species. Second, since reactions between RDX and its decomposition products can lead to changes in the composition of the sample being studied during the course of an experiment, it is important to determine how the gas formation rates of all the products change as a function of time during the experiment. Reactions that may control the decomposition of RDX by itself may not control its decomposition in the presence of its decomposition products. Obtaining this information on the decomposition products should further our understanding of the decomposition of these materials and hopefully unravel some of the conflicting results that have been observed using more conventional experimental techniques.

Previously, we have used a combination of simultaneous thermogravimetric modulated beam mass spectrometry (STMBMS), TOF velocity-spectra analysis, and isotopic analogues of HMX to study the thermal decomposition mechanisms of HMX in the condensed phase below its melting point. From this work we have identified and measured the rates of formation of all the major thermal decomposition products formed during the decomposition of HMX. We have found that HMX decomposes via several parallel reaction pathways and that trapping of the HMX decomposition products within gas bubbles in the HMX particles plays a significant role in its decomposition mechanism. The reaction pathways that are consistent with both our measured rates of gas product formation¹ and our deuterium kinetic isotope effect (DKIE) and isotopic scrambling experiments² are as follows: (1) breaking of the N-N bond to form NO₂, followed by the elimination of the two remaining methylenenitramine (CH₂=N-NO₂) groups that subsequently decompose to CH₂O and N₂O, (2) a reaction mechanism that involves the transfer of a hydrogen atom during the rate-limiting step (H₂O trapped within the particle is one possible hydrogen containing species that may be involved in this reaction path), and (3) the formation of the mononitroso analogue of HMX (ONTNTA, III) within the solid HMX that



is consistent with the predominant lack of isotopic scrambling of the nitrogen atoms of ONTNTA found in the experiments with mixtures of ¹⁴N and ¹⁵N labeled HMX. Since these experiments with HMX were conducted 45-70 °C below its melting point, the decomposition products were trapped within the solid HMX

particles for long periods prior to their release. In contrast, the results on RDX that we present in this paper for the most part occur in the liquid phase, and the release of the decomposition products from the sample is more rapid than in the experiments with solid-phase HMX. The results of the thermal decomposition of RDX in the liquid phase will be shown to indicate that four different primary reaction pathways control its decomposition, and there are significant differences between its decomposition pathways and those of HMX in the solid phase.

In this paper and the following paper,²⁴ we examine the thermal decomposition reactions and the concomitant effect of physical state (i.e., solid vs liquid) that control the decomposition pathways of RDX and compare the results to those found for the decomposition of HMX. We present in this paper the results from experiments with RDX that are used to identify the decomposition products from the mass spectrometry data, provide the temporal dependence of the rates of formation of the various decomposition products formed in solid, liquid, and mixed-melt phases of RDX, and discuss the primary reaction pathways that control the thermal decomposition of RDX. The following paper contains data on the probable rate-limiting steps and important bond-breaking processes derived from the DKIE and isotopic scrambling results from decomposition of isotopic analogues of RDX and discusses the implications of these results on the reactions that occur in each of the primary reaction pathways.

Experimental Section

Instrument Description. The STMBMS apparatus and the basic data analysis procedures have been described previously.^{25,26} Briefly, this instrument allows the concentration and rate of formation of each gas-phase species in a reaction cell to be measured as a function of time by correlating the ion signals at different *m/z* values measured with a mass spectrometer with the force measured by a microbalance at any instant. In the experimental procedure, a small sample (~10 mg) is placed in an alumina reaction cell that is then mounted on a thermocouple probe that is seated in a microbalance. The reaction cell is enclosed in a high vacuum environment (<10⁻⁶ Torr) and is radiatively heated by a bifilar-wound tungsten wire on an alumina tube. The molecules from the gaseous mixture in the reaction cell exit through a small diameter (~25 μm in these experiments) orifice in the cap of the reaction cell, traverse two beam-defining orifices before entering the electron-bombardment ionizer of the mass spectrometer where the ions are created by collisions of electrons with the different molecules in the gas flow. The background pressures in the vacuum chambers are sufficiently low to eliminate significant scattering between molecules from the reaction cell and background molecules in the vacuum chambers. The different *m/z*-value ions are scanned with a quadrupole mass filter and counted with an ion counter. The gas flow is modulated with a chopping wheel, and only the modulated ion signal is recorded. The containment time of gas in the reaction cell is a function of the area of the orifice, the free volume within the reaction cell, and the characteristics of the flow of gas through the orifice. For the reaction cell used in the experiments with RDX, the time constant for exhausting gas from the cell (i.e., the time it takes after its formation, for a gaseous product to exit from the reaction cell) is short (~3.2 s) compared to the duration of the experiments (>~1000 s). Since the evaporation rate of the reactant is controlled by the size of the reaction cell orifice, the relative rates of reactant evaporation and reactant decomposition are controlled by adjusting the size of the reaction cell orifice.

Two different types of reaction cells are used in the experiments. Both types are constructed from high density alumina. A new design has been developed to reduce the rate of evaporation of RDX and also to prevent the clogging of the exit orifice due to splattering of molten RDX, as experienced with the previous design.²⁷ A cross section of the new reaction cell design is shown in Figure 1. The orifice assembly consists of a hole located in the center of a 25.4 μm thick gold foil disk that is sandwiched between two alumina containment plates. The orifice assembly is sealed to the reaction cell with a ground cone fit. A hollow

TABLE I: Experimental Parameters

parameter	experiment no.						
	I	II	III	IV	V	VI	VII
RDX preparation ^a	pure	pure d_6	Mil	pure	pure	Mil	Mil
sample weight (mg)	3.95	7.27	7.81	6.50	29.2	8.97	8.50
reaction cell type ^b	2	2	2	2	1	1	1
orifice diameter (μm)	25.4	25.4	25.4	25.4	10.2	53	53
temperature ($^{\circ}\text{C}$)	195–215	195–215	180–225	193	190	192	190–205
heating rate ($^{\circ}\text{C}/\text{min}$)	0.58	0.58	0.54	isothermal	isothermal	isothermal	0.56
ionizer electron energy (eV)	18.4	18.4	20.4	20.4	18.4	18.4	18.4
experiment type ^c	quant	quant	quant	quant	ion	TOFVS	TOFVS

^aRDX denoted as pure or RDX- d_6 are pure samples of RDX prepared by the method outlined in ref 24. RDX denoted as Mil is prepared according to military standard Mil-R-398C Type B and contains 96% RDX and 4% HMX. ^bReaction cells denoted as 1 are constructed completely from alumina and are described in ref 26. Reaction cells denoted as 2 utilize a 25.4 μm thick gold pinhole orifice and are described in this paper. ^cQuant denotes a quantitative experiment to determine reaction rates, ion denotes only ion signals analyzed, and TOFVS denotes a time-of-flight velocity-spectra experiment.

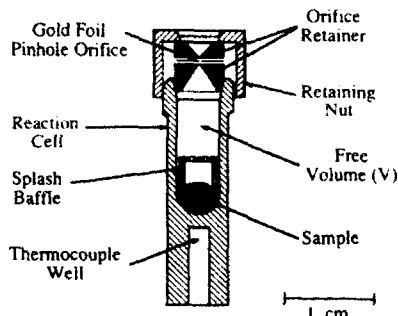


Figure 1. Cross section of the reaction cell used for thermal decomposition experiments. Reaction cell is constructed from alumina and is cylindrically symmetric about the vertical axis through the center of the cell. Gas exhausts through the pinhole orifice located in the 25.4 μm thick gold foil.

cylindrical baffle with four holes in the top plate and constructed from alumina is placed over the sample inside the reaction cell to minimize the splattering of liquid RDX onto the exit orifice. The free volume within the cell is 0.256 cm^3 .

The mass range of the mass spectrometer is calibrated using perfluorotributylamine, and the resolution is set so that the peak widths in the 20–300 amu region are approximately 0.7 amu full width at 10% maximum. The ionizer is operated in the linear electron-emission range at 1.0 mA. The electron energy is calibrated using the appearance potentials of H_2 and H_2O . The specific electron energies used for each experiment are listed along with other experimental parameters in Table I.

Identification of Decomposition Products. The decomposition products are identified by (1) using isotopically labeled analogues of RDX to determine the formulas of the m/z values measured with the mass spectrometer, (2) performing an autocorrelation analysis on all of the ion signals measured during one thermal decomposition experiment and separating the different m/z values into temporally correlated groups that represent the major ion signals in the mass spectra of each product, and (3) measuring TOF velocity spectra of ion signals at m/z values representing each decomposition product to determine the molecular weight of the respective thermal decomposition product. Explicit details of this procedure have been described previously for the case of HMX decomposition.²⁶

Quantification Procedure. The procedures used to convert the ion signals measured with the mass spectrometer to rates of gaseous decomposition product formation have also been described previously.^{25,27} After the mass spectrometer sensitivity factors are determined, the results are expressed as either the number density, partial pressure or the rate of molar gaseous product formation of each species as a function of time. For decomposition products that are present only in the gas phase and have low solubilities in the condensed phase, the rates of release from the reaction cell are equal to the rates of formation of these decomposition products. For products that are present in both the gas and condensed phases, the rate of release from the reaction cell

is determined by the equilibrium vapor pressure of the species in the reaction cell.

Sample Preparation. The pure RDX and deuterium labeled analogue of RDX (RDX- d_6) are prepared by oxidation of 1,3,5-trinitrosohexahydro-*s*-triazine following the procedure described in the accompanying paper.²⁴ The mean particle diameter of RDX used in these experiments is 130 μm . The lower purity RDX sample is prepared according to military specification MIL-R-398C Type B and contains approximately 4% HMX.

Results

Identification of Decomposition Products. The m/z values associated with the various thermal decomposition products formed from unlabeled and ^2H , ^{13}C , and ^{15}N labeled RDX are shown in Table II. The formulas for the ion signals of m/z values associated with the lower molecular weight products are as expected from the unlabeled and isotopically labeled RDX analogues. These products include H_2O , HCN , CO , CH_2O , NO , N_2O , and NO_2 . The results from the isotopically labeled RDX show that the formula for the ion signal at $m/z = 45$ is H_2NCHO and is probably formamide. Likewise, the results also show that the formula that corresponds to $m/z = 59$ is CH_3NHCHO and is most likely *N*-methylformamide. The ion signals from unlabeled RDX at m/z values of 70 and 97 are temporally correlated and originate from the same product. The results from experiments with the isotopic analogues of RDX show that the formula of the $m/z = 70$ ion is $\text{C}_2\text{H}_2\text{N}_2\text{O}$ and the formula of the $m/z = 97$ ion is $\text{C}_3\text{H}_3\text{N}_3\text{O}$. Finally, the ion signals at m/z values of 42 and 132 are temporally correlated. The results from the experiments with the isotopic analogues of RDX show that the ion formula for $m/z = 132$ is $\text{C}_2\text{H}_4\text{N}_2(\text{NO})\text{NO}_2$.

TOF spectra in Figure 2 show that ion signals at some of the m/z values arise solely from the thermal decomposition products. These products include HCN ($m/z = 27$), N_2O ($m/z = 44$), methylformamide H_2NCHO ($m/z = 45$), HONO ($m/z = 47$), and $\text{C}_3\text{H}_3\text{N}_3\text{O}$ ($m/z = 97$). On the other hand, TOF velocity spectra of ion signals at several other m/z values show that the ion signals at these m/z values arise from a decomposition product in addition to RDX that evaporates from the reaction cell without undergoing decomposition. Contributions from both RDX and its decomposition products are found at m/z values associated with CO ($m/z = 28$), CH_2O ($m/z = 29, 30$), NO ($m/z = 30$), and NO_2 ($m/z = 46$). Finally, the TOF velocity spectra show that ion signals at several m/z values are daughter ions formed in the mass spectrometer from thermal decomposition products (e.g. 132). These include the ion signal at $m/z = 58$ that probably originates from the *N*-methylformamide dimer (MW = 118), the ion signal at $m/z = 70$ that originates from the $\text{C}_3\text{H}_3\text{N}_3\text{O}$ product, and the ion signal at $m/z = 132$ that originates from 1-nitroso-3,5-dinitrohexahydro-*s*-triazine (ONDNTA) (MW = 206).

Several of the TOF velocity spectra displayed in Figure 3 show that the major ion signals recorded at several m/z values are formed solely from evaporating RDX. These spectra were collected during the isothermal decomposition of RDX under the conditions listed for experiment VI in Table I. The TOF velocity

TABLE II: Ion Formulas, m/z Values from Isotopically Labeled Analogues, and Pyrolysis Product Molecular Weights and Formulas from the Thermal Decomposition of RDX

ion formula	m/z values ^a				pyrolysis product molecular weight ^b	pyrolysis product formula
	ul	d_6	^{13}C	$^{15}\text{N}_6$		
H ₂ O	18	20	18	18	18	H ₂ O
HCN	27	28	28	28	27	HCN
CO	28	28	29	28	28, 222	CO, RDX
CHO	29	30	30	29	30, 222	CH ₂ O, RDX
CH ₂ O	30	32	31	30	30, 222	CH ₂ O, RDX
NO	30	30	30	31	30, 222	NO, RDX
NCO	42	42	43	43	206, 222	ONDNTA, RDX
N ₂ O	44	44	44	46	44	N ₂ O
H ₂ NCHO	45	48	46	46	45	H ₂ NCHO
NO ₂	46	46	46	47	46, 222	NO ₂ , RDX
HONO	47	48	47	48	47	HONO
CH ₃ NHCHO	59	64	61	60	118	(CH ₃ NHCHO) ₂
C ₂ H ₃ N ₂ O	70	72	72	72	97	C ₂ H ₃ N ₂ O
C ₂ H ₃ N ₂ O	97	100	100	100	97	C ₂ H ₃ N ₂ O
C ₂ H ₄ N ₂ (NO)(NO ₂)	132	136	134	136	206	C ₂ H ₄ N ₂ O ₂

^a The m/z values measured in thermal decomposition experiments with unlabeled (ul), deuterium-labeled (d_6), ^{13}C -labeled, and ^{15}N -labeled analogues of RDX. The experimental parameters used for ^{13}C - and ^{15}N -labeled samples were identical to those used for experiments I-III in Table I.

^b The molecular weights of the compounds contributing to the ion signal at each m/z value are determined from TOF velocity spectra.

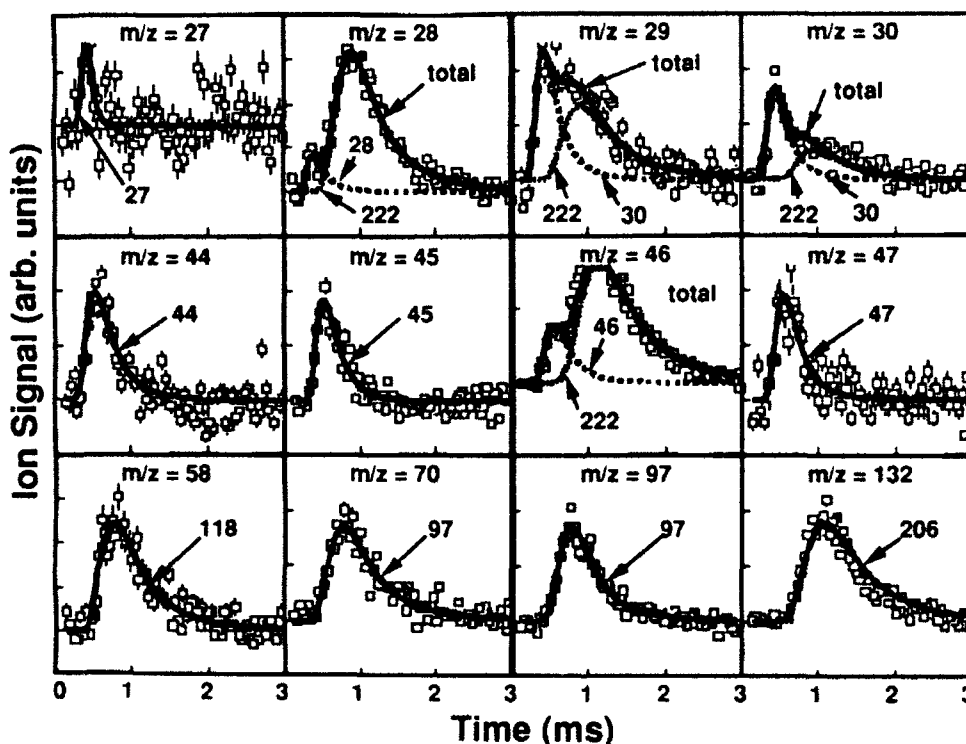


Figure 2. Time-of-flight velocity spectra of ion signals at various m/z values measured with the mass spectrometer. The signals are formed from the mixture of products evolving from the reaction cell during the decomposition of RDX. The symbols represent the measured data, the error bars denote the 1σ standard deviation, and the solid and dashed curves represent the contribution to the ion signals from the various species (denoted by their molecular weights) that are contained in the mixture of products flowing out of the reaction cell during the decomposition. The details of the deconvolution procedure to fit the data are described in ref 26. TOF velocity spectra at m/z values of 30, 44, 46, 70, 97, and 132 were collected in experiment VI where the sample temperature was 192 °C. The remaining spectra were collected in experiment VII where the reaction cell temperature was 197 °C for m/z values of 27, 28, and 29 and 201 °C for m/z values of 45, 47, and 58.

spectra at m/z values of 74, 75, 120, 128, and 148 clearly show that these ion signals originate from the electron-bombardment ionization of RDX followed by the fragmentation of the RDX molecular ion into its daughters. If thermal decomposition products are present at any of these m/z values, they are masked by the large signals originating from evaporating RDX. In light of the low electron energies (18.4 eV) used in these experiments and the significant fragmentation of HMX found in experiments with HMX,²⁶ this limitation is likely to be present in any thermal decomposition experiment that utilizes electron-bombardment ionization mass spectrometry to measure the mixture of decomposition products directly from a sample of RDX. In contrast, the IRMPD experiments²³ with a molecular beam of RDX util-

the kinematics of the dissociation reaction to separate the decomposition products from RDX in the molecular beam and therefore has been able to detect short-lived decomposition species from RDX such as methylenetrinitramine ($\text{CH}_2=\text{N}-\text{NO}_2$).

In addition to the more commonly observed thermal decomposition products from RDX (HCN, CO, CH₂O, NO, N₂O, and NO₂), several other products have been observed. Most of the conventional mass spectrometry¹¹⁻¹⁵ and infrared¹⁷ measurements made on the decomposition of RDX have not usually reported the formation of water as a major decomposition product, due to interference of background water in the instrument. The use of the modulated molecular beam mass spectrometry detection technique along with the use of deuterium labeled RDX have

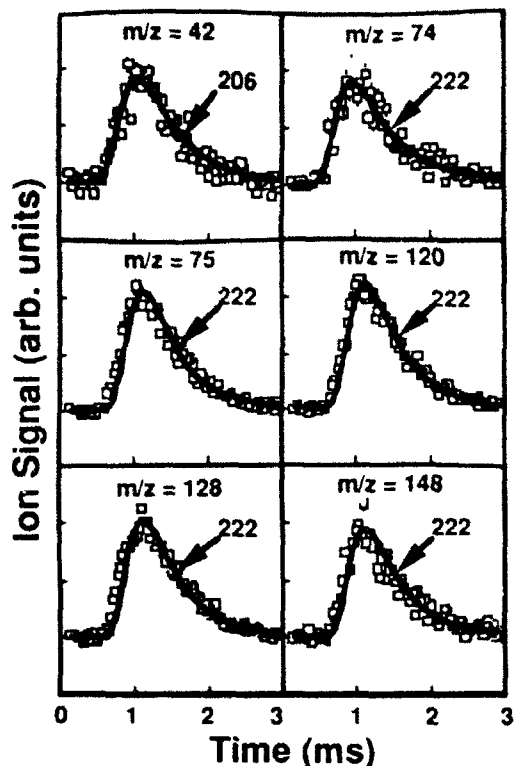
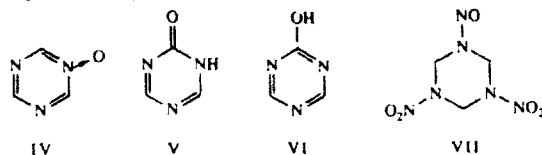


Figure 3. Time-of-flight velocity spectra of ion signals at various m/z values measured with the mass spectrometer. The signals are formed from the mixture of products evolving from the reaction cell during the decomposition of RDX. The symbols represent the measured data, the error bars denote the 1σ standard deviation, and the solid and dashed curves represent the contribution to the ion signals from the various species (denoted by their molecular weights) that are contained in the mixture of products flowing out of the reaction cell during the decomposition. The TOF velocity spectra at m/z values of 42, 75, 120, 128, and 148 were collected in experiment VI where the sample temperature was 192 °C and the spectra at $m/z = 74$ was collected in experiment VII at a temperature of 195 °C.

shown that water is a major thermal decomposition product.

The $C_3H_3N_3O$ ($m/z = 97$) product is one of the higher molecular weight thermal decomposition products formed from RDX. Since it was first observed,²⁸ a subsequent study using tandem mass spectrometry²⁹ has claimed that two structures (IV and V)



are consistent with the above formula, to which a third structure (VI) may, in fact, be added. Since the exact structure of this compound is not presently known, it is referred to as oxy-*s*-triazine (OST).

Another higher molecular weight thermal decomposition product formed from RDX is ONDNTA (VII). The two largest ion signals formed from ONDNTA are at m/z values of 42 and 132. The TOF velocity spectra for these two m/z values, which are displayed in Figures 2 and 3, clearly show that the molecular weight of the thermal decomposition product associated with these ion signals is approximately 206. Furthermore, a small ion signal at $m/z = 206$ that is temporally correlated with the ion signals at $m/z = 42$ and 132 is the ONDNTA molecular ion. Previous mass spectrometry studies of RDX decomposition have observed ion signals at $m/z = 132$ ¹¹ but were unable to identify the thermal decomposition product leading to the formation of this ion in the mass spectrometer.

The final group of products that we have identified consists of several different formamides. We have observed ion signals corresponding to NH_2CHO ($m/z = 45$), $(CH_3)NHCHO$ (m/z

$= 58, 59$), and a smaller ion signal corresponding to $(CH_3)_2NCHO$ ($m/z = 73$). The TOF velocity spectra displayed in Figure 2 show that the molecular weight of the thermal decomposition product forming the ion signal at $m/z = 45$ is consistent with the formamide product. The TOF velocity spectra of the ion signal at $m/z = 58$ show that this product has a molecular weight of approximately 118 and together with the formula of the ions as determined from the correlation of the m/z values between the various isotopic analogues of RDX suggest that this product is *N*-methylformamide that evolves as a dimer from the reaction cell. The ion signal at $m/z = 73$ is small, and TOF velocity spectra were not collected. The structural assignments of these products are consistent with the previous tandem mass spectrometry studies of Snyder et al.²⁷ One product that is formed during the decomposition, and not observed with the mass spectrometer, is an orange-brown residue that coats the inner walls of the reaction cell.

Rates of Formation of Thermal Decomposition Products. In addition to providing the identities of the decomposition products formed from RDX, the results also provide the rates of release of each individual product from the reaction cell as described above under the "Quantification Procedure".

The results from four experiments (experiments I-IV) illustrate the effect of melting on the decomposition of RDX and show the presence of several different reaction branches that control the thermal decomposition of RDX. The series of experiments include two thermal ramp experiments with pure RDX (experiment I with pure RDX and experiment II with RDX-*d*₆), one thermal ramp experiment with an RDX/4% HMX mixture (experiment III) that forms a lower melting eutectic, and two isothermal experiments with pure RDX (experiments IV and V) held below its melting point. The analysis of the data from experiments I-IV was carried out in the manner described above, and the results are presented in Table III. As shown in Table III, the mass balance for carbon, hydrogen, nitrogen, and oxygen is within 2% of nominal for experiments I-III. Table III also lists the amount of each product formed during each experiment and the ratio of the total amount of each product formed to the amount of RDX that decomposed.

The temporal behaviors of the gas formation rates of the thermal decomposition products from pure RDX (experiment I) and RDX-*d*₆ (experiment II) are shown in Figures 4 and 5, respectively. The gas formation rates of the decomposition products are divided into three groups for each experiment based on differences in their temporal behaviors. The products in the first group are shown in the panel A of Figures 4 and 5 and consist of the OST, H₂O, NO, and HCN thermal decomposition products. The general behaviors exhibited by these products include a very rapid rise from zero in their gas formation rates as the RDX melts, the maximum rate of gas formation immediately after melting, and a decrease in the rate of gas formation of OST, H₂O, and NO as the amount of RDX in the reaction cell diminishes. Furthermore, in these two experiments, and many other experiments with pure RDX, the following general features were observed in the OST, H₂O, and NO gas formation rates: (1) the OST, H₂O, and NO showed a sharp peak after the sample melted; (2) following the sharp peak, the OST gas formation rate gradually declined as the amount of RDX sample remaining diminished; and (3) following the sharp peak, the H₂O and NO gas formation rates rose to form a second broader peak or a shoulder and then also declined as the amount of RDX sample remaining diminished.

The products in the second group are shown in panel B in Figures 4 and 5 and consist of N₂O, CH₂O, CO, NO₂, and NH₂CHO. The general behaviors exhibited by these products include a rapid rise from zero in their rates of gas formation as the sample melts followed by a more gradual rise to a very broad peak or plateau in their gas formation rates as the amount of RDX remaining decreases. The gas formation rates of N₂O and CH₂O remain at high levels even when the amount of RDX has greatly diminished near the end of the experiment. It is clear that the gas formation rates of these products are not simply proportional to the amount of RDX present as is the case with OST, H₂O, and

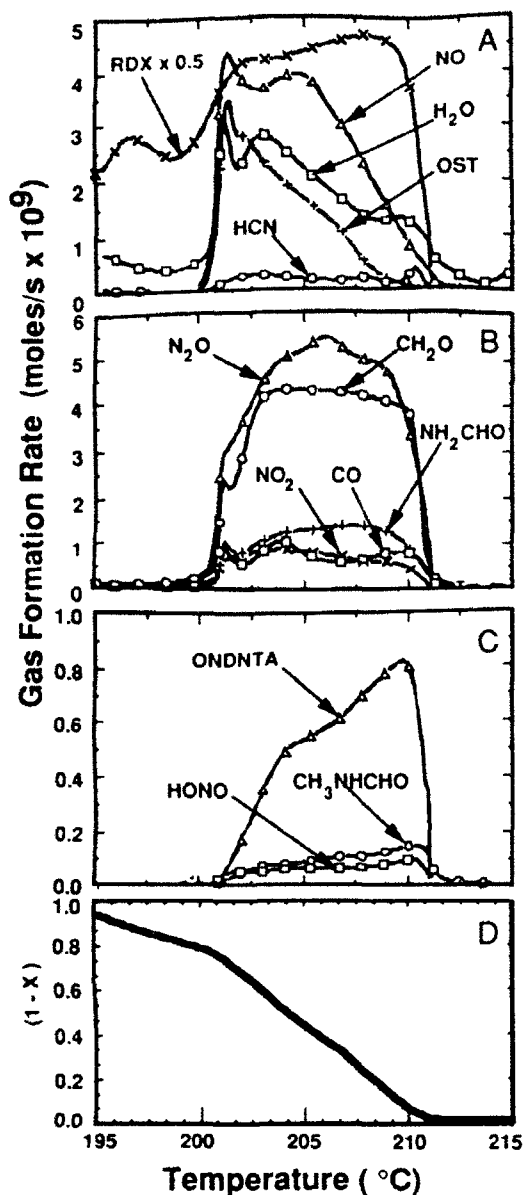


Figure 4. Gas formation rates of the thermal decomposition products formed during experiment I using pure unlabeled RDX and a heating rate of $0.58\text{ }^{\circ}\text{C}/\text{min}$. The gas formation rates of the products are divided into three groups with similar temporal behaviors: Panel A shows products whose gas formation rates peak after the sample melts and then remain approximately proportional to the amount of sample left in the reaction cell, panel B shows products whose gas formation rates peak between the onset of decomposition and the depletion of the sample, and panel C shows products whose gas formation rates keep increasing throughout the experiment until the sample is depleted. The weight fraction of the original sample $(1 - X)$ remaining in the reaction cell is shown in panel D.

NO. Since products formed from the decomposition of RDX in the gas phase would be proportional to its vapor pressure (3–6 Torr in these experiments), it is possible that N_2O and CH_2O are formed by this route. Results from previous gas-phase decomposition studies of RDX^{30} ($A = 10^{16}$, $E_a = 40.4\text{ kcal/mol}$) indicate that between 5 and 10% of the N_2O formed after the RDX melts may arise from decomposition in the gas phase. However, these same results and the assumption that each gas-phase RDX molecule decomposes to form two N_2O molecules show that the formation rates of N_2O prior to melting is overestimated by at least a factor of 2 when compared to the N_2O gas formation rates prior to melting in our experiments. This is illustrated in Figures 4 and 5 by the relatively low gas formation rates of N_2O prior to melting (panel B) compared to the smaller change in the vapor pressure of RDX as the sample melts (panel A). This is reasonable

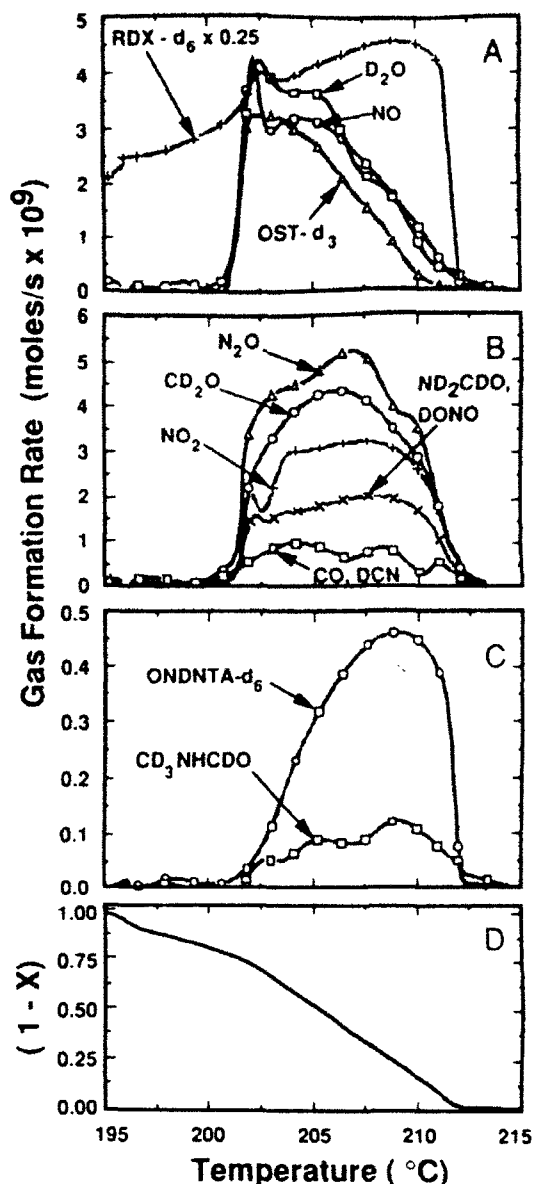


Figure 5. Gas formation rates of the thermal decomposition products formed during experiment II using pure RDX-d_6 and a heating rate of $0.58\text{ }^{\circ}\text{C}/\text{min}$. The gas formation rates of the products are divided into three groups with similar temporal behaviors: Panel A shows products whose gas formation rates peak after the sample melts and then remain approximately proportional to the amount of sample left in the reaction cell, panel B shows products whose gas formation rates peak between the onset of decomposition and the depletion of the sample, and panel C shows products whose gas formation rates keep increasing throughout the experiment until the sample is depleted. The weight fraction of the original sample $(1 - X)$ remaining in the reaction cell is shown in panel D.

since the fraction of gas-phase RDX is small ($\sim 2 \times 10^{-3}$) in these experiments. Consequently, it appears that the rates of formation of products in this group may be a result of either "autocatalytic" reactions or reactions between RDX and its own decomposition products.

The products in the third group are shown in panel C of Figures 4 and 5 and consist of ONDNTA, HONO, and *N*-methylformamide. The general behaviors of the products in this group differ from the previous two groups. The products in this group do not exhibit a rapid rise in their rates of gas formation when the sample melts. Instead their rates of gas formation rise slowly from zero to a peak when the sample is almost completely depleted. This suggests that these components may be soluble in, or derived from a product that is soluble in, RDX and that their release rates from the reaction cell may be dependent on their vapor pressures which

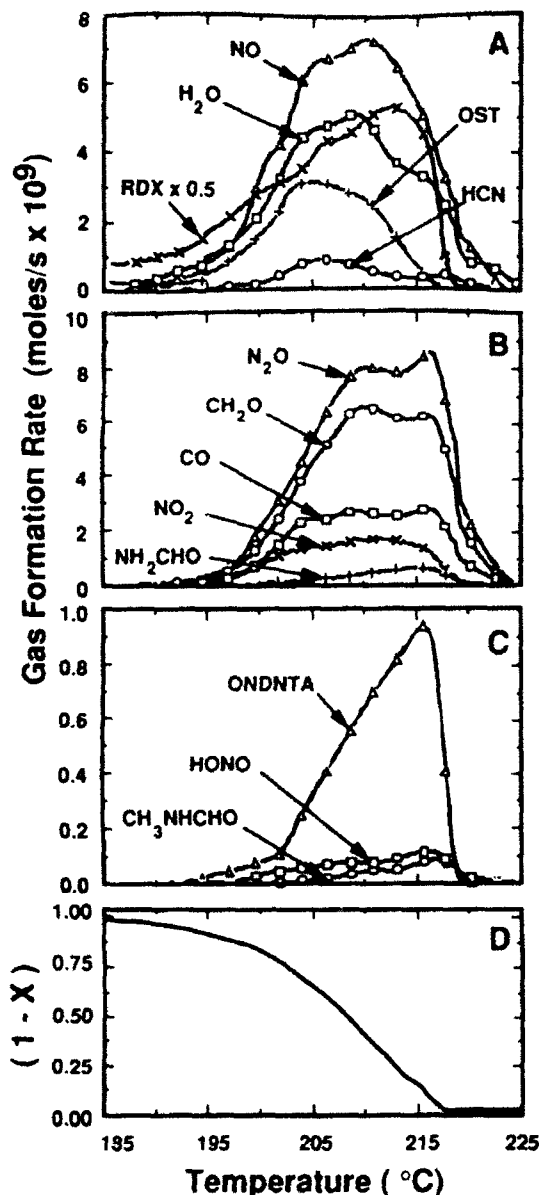


Figure 6. Gas formation rates of the thermal decomposition products formed during experiment III using RDX that contains approximately 4% HMX and a heating rate of 0.54 °C/min. The gas formation rates of the products are divided into three groups with similar temporal behaviors: Panel A shows products whose gas formation rate rises from zero at 188 °C, gradually increases and peaks first during the decomposition, panel B shows products whose gas formation rates peak later than the first group but prior to the depletion of the sample, and panel C shows products whose gas formation rates keep increasing throughout the experiment until the sample is depleted. The weight fraction of the original sample $(1 - X)$ remaining in the reaction cell is shown in panel D.

in turn are dependent on their mole fractions in the solution.

The gas formation rates of the products formed during the decomposition of the RDX/4% HMX sample (experiment III) are shown in Figure 6. In a manner similar to experiments I and II, the results are also divided into the same three groups as in Figures 4 and 5 that depend on the temporal behaviors of the products. The general sequence of release of the products in each group is the same as that for the pure RDX and RDX- d_6 . The products in the first group are released first, and their gas formation rates are proportional to the amount of RDX remaining in the experiment. The gas formation rate of products in the second group increase later than the first group and gradually increase and remain at a constant gas formation rate until the sample is depleted. The gas formation rates of the third group of products increase constantly until the sample is depleted.

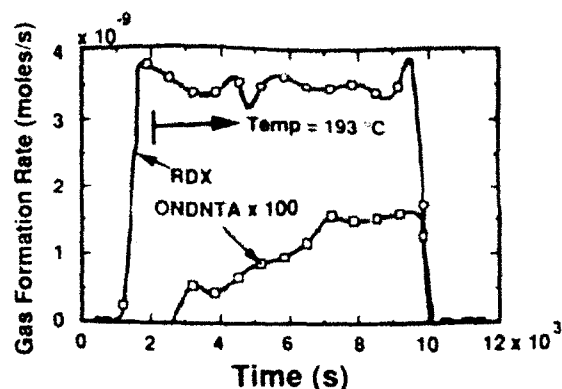


Figure 7. Gas formation rate of the ONDN TA formed during experiment IV using pure unlabeled RDX and the release rate of RDX. The arrow pointing to the right starts at the time that the isothermal temperature of 193 °C is first attained. The only product observed during this experiment is ONDN TA.

However in contrast to the behaviors of the gas formation rates with the pure RDX and RDX- d_6 , the temporal behaviors of the products within the groups differ. The first difference is that the evolution of products in all of the groups starts at lower temperatures than those observed in the experiments with pure RDX and RDX- d_6 . For example, the evolution of OST, H₂O, and NO starts at 188 °C and the evolution of CO, CH₂O, N₂O, NO₂, and NH₂CHO starts at 193 °C. Another difference between the gas evolution rates is the absence of an abrupt increase in the gas formation rates of the products that coincides with melting of the sample as seen in the experiments with pure RDX and RDX- d_6 . Since the mixture of RDX/4% HMX is known to form a lower melting eutectic that melts over a wider temperature range, the results are consistent with the thermal decomposition rate of RDX being much higher in the liquid phase than in the solid phase.

Comparison of the behaviors of the gas formation rates of the decomposition products from pure RDX and RDX- d_6 with the behaviors of the gas formation rates of the products from RDX/4% HMX in the vicinity of the melting point of RDX (201 °C) raises the question of whether there is significant decomposition of RDX in the solid phase. For example, in the experiment with pure RDX it is possible that RDX undergoes decomposition in the solid but that the products are trapped within the solid and not released at significant rates until the sample melts. To check whether there was decomposition within the solid prior to melting, an isothermal decomposition experiment with pure RDX was conducted at 193 °C (experiment IV) where no significant melting would have occurred. The results from this experiment are summarized in Table III and shown in Figure 7. The only product observed in this experiment is ONDN TA, and it was formed at very low rates. The data from experiment IV were analyzed for all of the other products observed in experiments I–III, and no other products were observed. Thus, these results show that the decomposition rate of RDX is very much lower in the solid phase than it is in the liquid phase. Furthermore, the results of experiment IV do not exhibit the accelerating decomposition rate observed previously with HMX.¹ This is due to the shorter length of time that the RDX sample used in experiment IV had to decompose in comparison to the previous experiments with HMX. To ascertain whether RDX exhibits the same type of decomposition behavior in the solid phase as HMX, larger samples of RDX were used in several experiments. The results of the isothermal decomposition of a 29.2-mg sample of pure RDX at 190 °C are shown in Figure 8. In this experiment only the ion signals at the m/z values representing each decomposition product are shown because as the larger samples start to decompose some of the liquid splatters and blocks the exit orifice making quantification of the results not possible. However, the results clearly show that RDX undergoes an accelerated release of the decomposition products. The products that are released during the induction period are ONDN TA, N₂O, and a small amount of formaldehyde. At approximately 20 000 s the decomposition rate accelerates and

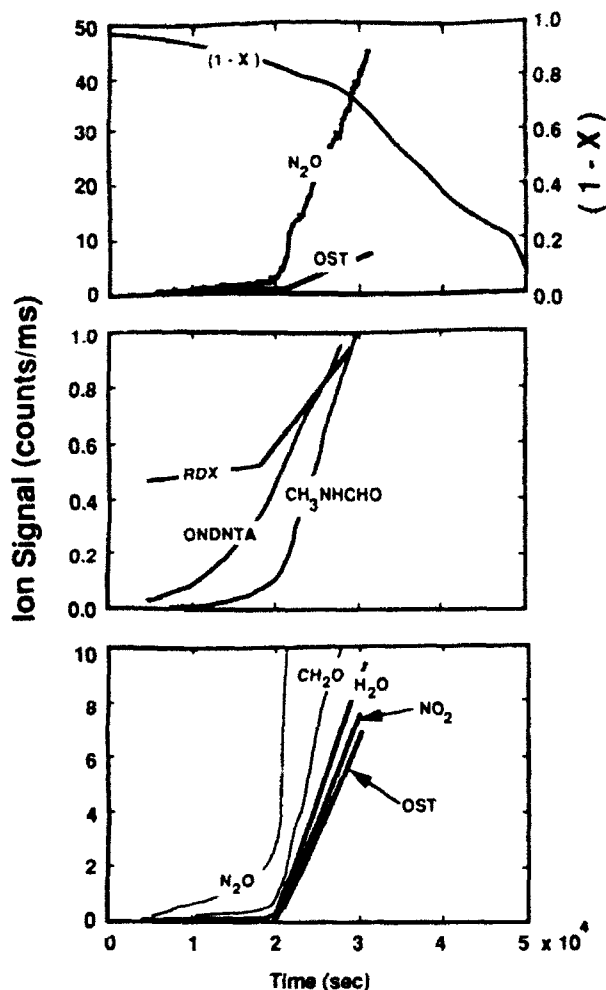


Figure 8. Ion signals associated with the thermal decomposition products formed during experiment V using pure unlabeled RDX at an isothermal temperature of 190 °C. $1 - X$ is the fraction of sample remaining. The ONDNNTA, N_2O , CH_2O , and CH_3NHCHO signals all show a gradual increase prior to the onset of the appearance of the signals associated with the liquid-phase decomposition (OST, H_2O , and NO_2). Ion signals past 30000 s are not shown due to clogging of the reaction cell orifice.

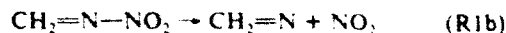
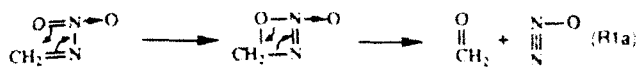
the evolution of OST, H_2O , NO , and NO_2 commences. Although the data from experiment V is not strictly quantitative, it is clear that the amount of N_2O formed compared to OST is much greater in the solid-phase decomposition than it is in the liquid-phase decomposition (since the relative ion formation probability is smaller for N_2O than OST, the ratio of N_2O to OST will be larger than the ratio of the ion signals of these two products shown in Figure 8).

Discussion

As stated in the Introduction, we discuss here the identity of the decomposition products of RDX above its melting point, their rates of formation, and the temporal correlations among them. Following this, four primary branches of the decomposition mechanism will be identified and discussed. Pyrolytic reactions predominantly occur via free radical pathways, but it should be borne in mind that during the later stages of the decomposition the presence of water produced during the reaction may give rise to contributions from ionic processes. More definitive conclusions about the mechanisms involved in the four primary branches and comparison to the previously published^{1,2} HMX decomposition chemistry will be deferred to the next paper,²⁴ in which insights into the bond-breaking processes are derived from additional experimental data on isotopic scrambling and deuterium kinetic isotope effects.

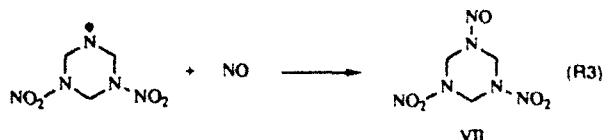
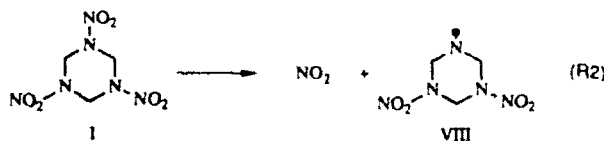
Lower Molecular Weight (Gaseous) Products. The nature and distribution of the low molecular weight (up to 47) products (H_2O ,

CH_2O , N_2O , NO , CO , and HCN) from RDX decomposition closely parallel those from HMX. In RDX small amounts of three additional ones, namely, NH_2CHO , NO_2 , and $HONO$ were detected. These were probably formed in the decomposition of HMX but were not observed because of secondary reactions within the HMX particle. Among the gaseous products, CH_2O and N_2O are the largest ones in both RDX and HMX but the ratio of $N_2O:CH_2O$ is larger in HMX. The amount of HCN formed is also larger in HMX. However, judging from the general similarities in products and the closely related structures of RDX and HMX, the reaction pathways previously suggested² for the gaseous products from HMX should also be valid for RDX. To recall, it has been assumed that CH_2O and N_2O , which are the major products, arise by a concerted process from each methylenenitramine unit in HMX:

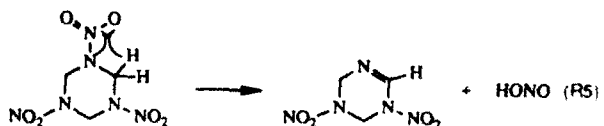
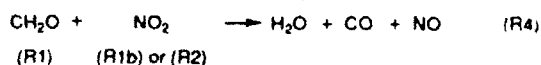


In both RDX and HMX the amount of N_2O formed corresponds approximately to the collapse of one less methylenenitramine unit than present in the respective molecules. This is consistent with the conclusion that the decomposition process probably commences with the "least energy" pathway, namely, the cleavage of an NO_2 group after which the rest of the methylenenitramine units collapse mostly to CH_2O and N_2O . This requires that the rates of formation of CH_2O and N_2O should be proportional to the amount of RDX at any given time. However, in Figure 4, panel B, the shapes of the gas formation rate curves are inconsistent with the expected decline in rate with the RDX consumed. This suggests that there are other sources for N_2O and CH_2O formation which will be discussed later (see below). The rates of formation of NO and H_2O , however, do exhibit the expected decline as RDX is consumed (panel A, Figure 4), suggesting that they are products from a different reaction pathway.

Larger Molecular Weight Products. In addition to the gaseous products, RDX forms three larger products, ONDNNTA, OST, and methylformamide, discussed briefly in Results. In the next paper,²⁴ ONDNNTA is shown to be formed by N-N bond cleavage followed by the recombination of the residual radical with NO from another reaction as shown in the following:



The source of NO in (R3) may be either NO_2 or $HONO$ as shown in the following. (R4) was previously reported in the literature.³¹



ONDNTA is structurally similar to ONDNNTA formed in the decomposition of HMX in that they both represent net loss of one oxygen atom from their respective structures. In the case of HMX,

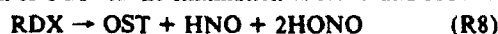
TABLE III: Quantitative Results from the Thermal Decomposition of RDX^a

species ^b	experiment no.							
	I		II		III		IV	
	amount (mg)	molar ratio	amount (mg)	molar ratio	amount (mg)	molar ratio	amount (mg)	
H ₂ O	0.054	0.70	0.058	0.74	0.192	0.85	0	
HCN	0.008	0.07	c	na	0.035	0.10	0	
CO	0.026	0.22	0.027	0.22	0.156	0.45	0	
CH ₂ O	0.128	0.99	0.127	0.97	0.366	0.98	0	
NO	0.1	0.77	0.082	0.63	0.422	1.13	0	
N ₂ O	0.221	1.17	0.206	1.07	0.68	1.24	0	
H ₂ NCHO	0.057	0.29	0.095	0.48	0.039	0.07	0	
NO ₂	0.037	0.19	0.144	0.72	0.146	0.25	0	
HONO	0.004	0.02	c	na	0.009	0.02	0	
CH ₃ NHCHO	0.007	0.03	0.006	0.02	0.006	0.01	0	
OST	0.157	0.38	0.201	0.48	0.485	0.40	0	
ONDNTA	0.118	0.13	0.079	0.09	0.232	0.09	0.016	
RDX	2.993	3.13	6.302	6.51	5.036	1.82	6.484	
mass balance								
%H	101.6				98.6			
%D			100.8					
%C	101.2		100.8		101.0			
%N	98.5		99.3		98.8			
%O	98.4		100.3		100.6			

^aThe conditions for each experiment are given in Table I. ^bThe species refer to either the listed species or its deuterium-labeled analogue where appropriate. ^cThese relatively minor species are masked by overlap of ion signals from CO and H₂NCHO that occur at the same *m/z* values as the deuterium-labeled analogues of these products.

it was suggested by the incomplete nitrogen isotope scrambling that ONTNTA formation was the result of N-N bond cleavage followed by reaction of NO₂ to form NO and recombination of the NO with the residual amine radical in the HMX lattice cage. However, this does not rule out the contribution from simple N-O bond cleavage in HMX.

Oxy-*s*-triazine (OST), represented by one of the three structures IV-VI, is a unique and significant (0.38 mol/(mol of RDX decomposed), Table III) product from RDX with no counterpart in solid-phase HMX decomposition. Structures V and VI actually represent tautomers. A plausible reaction scheme to rationalize the formation of OST via the elimination of HNO and HONO



is presented in the following paper.

Methylformamide is a minor product in the decompositions of both RDX and HMX, but it is, nevertheless, indicative of an important reaction pathway leading to a polyamide type of residue formation in both:

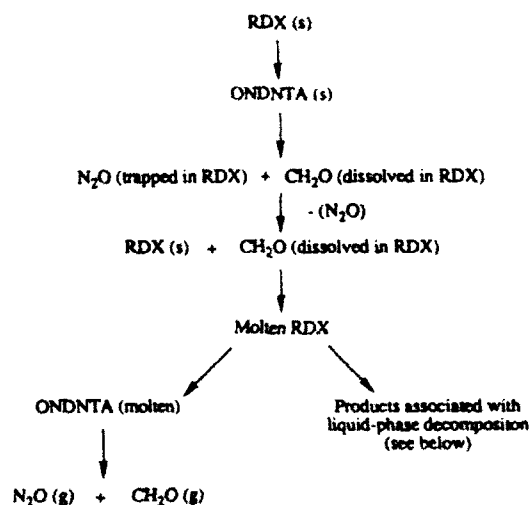


Decomposition Pathways. The temporal behaviors of the gas formation rates of the thermal decomposition products formed from RDX provide insight into the reaction pathways that lead to the formation of the various products. First we compare the rates of decomposition in the solid and liquid phases of RDX, and then we discuss the primary decomposition channels that lead to the formation of the observed products in both phases.

Liquid vs Solid-Phase Decomposition. The results clearly show that the rate of decomposition is much higher in the liquid phase than in the solid phase. For example, in the experiments with both pure and RDX-*d*₆, essentially no products appear until the sample starts to melt, at which time there is a rapid increase in the rate of formation of the decomposition products. The rate of increase in the gas formation rates of several of the products is determined by the increasing amount of liquid RDX present as the sample melts over a temperature range of approximately 1 °C. Further evidence for the rate of decomposition being proportional to the amount of liquid is observed in the decomposition of the RDX/4% HMX sample. In this case the sample

starts to melt at a lower temperature (188 °C) and melts over a broader temperature range. The more gradual increase in the amount of liquid RDX present as the sample is heated manifests itself in a more gradual increase in the rate of formation (and release) of the decomposition products (Figure 6).

Solid-Phase Decomposition. The results from the isothermal decomposition of solid-phase RDX (experiment V, Figure 8) exhibit the classic induction and acceleratory features that are characteristic of solid-phase decomposition reactions. This behavior is similar to that found in the decomposition of solid-phase HMX.¹ The temporal behaviors of the gas formation rates of the various products are controlled by condensed-phase decomposition reactions and changes in the physical state of the sample and can be summarized as follows:



The solid-phase RDX forms ONDNTA that subsequently decomposes predominantly to N₂O and CH₂O that remain trapped in the solid. As the build up of CH₂O and N₂O continues, N₂O is released from the sample and CH₂O disperses in the solid RDX causing the lattice structure of RDX to weaken, leading to the formation of molten RDX and the more rapid reactions associated with the liquid-phase decomposition. This decomposition pathway is consistent with the appearance of only ONDNTA, N₂O, and CH₂O prior to the start of the acceleratory stage. In addition, the fact that the release rate of N₂O is greater than that of CH₂O during the induction stage (see Figure 8) is consistent with the dispersion of CH₂O in the RDX lattice. The formation of

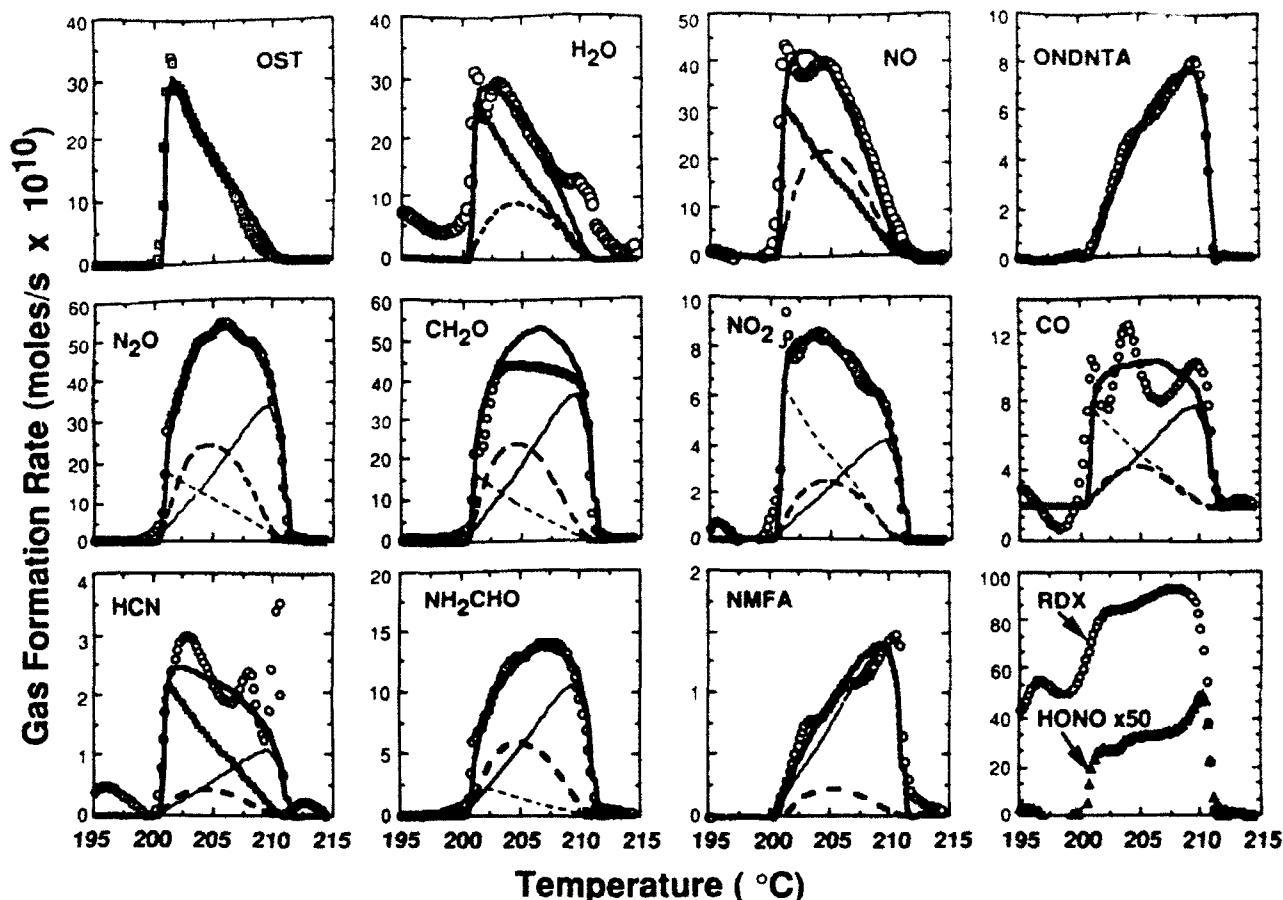


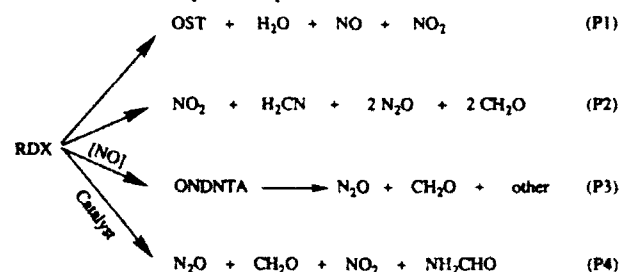
Figure 9. Gas formation rates of the products formed in experiment I with unlabeled RDX along with the fits to the data based on the four primary decomposition pathways. The bold line (—) in all of the graphs represents the total contribution from all of the reaction channels. The bold line (—) in OST and the square-dot lines for H₂O, HCN, and NO represent the contribution by reaction pathway P1. The thin dashed (---) lines shown in N₂O, CH₂O, NO₂, CO, HCN, and NH₂CHO represent the contributions from reaction pathway P2. The bold dashed lines (---) represent the contribution from the ONDNNTA decomposition pathway P3. The thin solid lines (—) that peak near the highest temperature correspond to the contribution from the catalytic decomposition pathway P4. The fit to the CH₂O data uses the same coefficients as those used to fit the N₂O data thus assuming that CH₂O and N₂O are formed in equal amounts. The difference between the calculated and measured gas formation rates for CH₂O indicates the amount of CH₂O that reacts prior to leaving the reaction cell.

ONDNTA in the solid is analogous to the formation of ONTNTA in the solid-phase decomposition of HMX. In isotopic scrambling work with solid-phase HMX,² it was found that only 25% of the ONTNTA product formed participated in scrambling of the NO group that replaced the NO₂ group. This lack of complete scrambling in HMX contrasts with the complete scrambling observed in the formation of ONDNNTA in liquid RDX and was ascribed to the formation of ONTNTA in the crystal lattice of HMX. Thus, from similarity of the results from experiment V and those of HMX, it appears that RDX also forms a mononitroso analogue, ONDNNTA, in the crystal lattice.

The acceleratory behavior of RDX, like that observed in the experiments with solid HMX, has been observed in many previous studies³ on HMX and RDX decomposition. In much of this work the effect has been described as "autocatalysis". However, from our results it appears that a large part of the acceleratory effect in the solid-phase decomposition most likely arises from a phase change from solid to liquid and not from catalysis of the reaction in the conventional sense.

Liquid-Phase Decomposition. The temporal behaviors of the gas formation rates of the decomposition products formed during the decomposition of RDX in the liquid phase exhibit a complex behavior that is determined by the formation of products from several different parallel reaction channels. The temporal behaviors of the data have been examined in light of the various reaction channels (reactions R1–R12) that were developed on the basis of the identity of the decomposition products. This effort has led to the development of a simple decomposition model that

requires the following four primary reaction channels to predict the main features of the temporal behaviors of the gas formation rates of the decomposition products.



The reaction pathways, P1–P4 denote the products that are associated with each channel. The products associated with each pathway may be formed by a series of reactions. For example, the products in pathway P1 may be formed via reaction R8 followed by the reaction of HONO by either reaction R6 or R7. Since the reactions that comprise these four reaction pathways occur in the liquid phase and generate products that can undergo further reactions prior to their measurement, it is not possible at this time to determine their exact details. However, the data do establish these pathways as major decomposition routes that control the decomposition of RDX in the liquid phase.

Simple Model for the Four Primary Reaction Pathways. The contribution of each of these reaction pathways to the various decomposition products is shown in Figure 9 for pure RDX

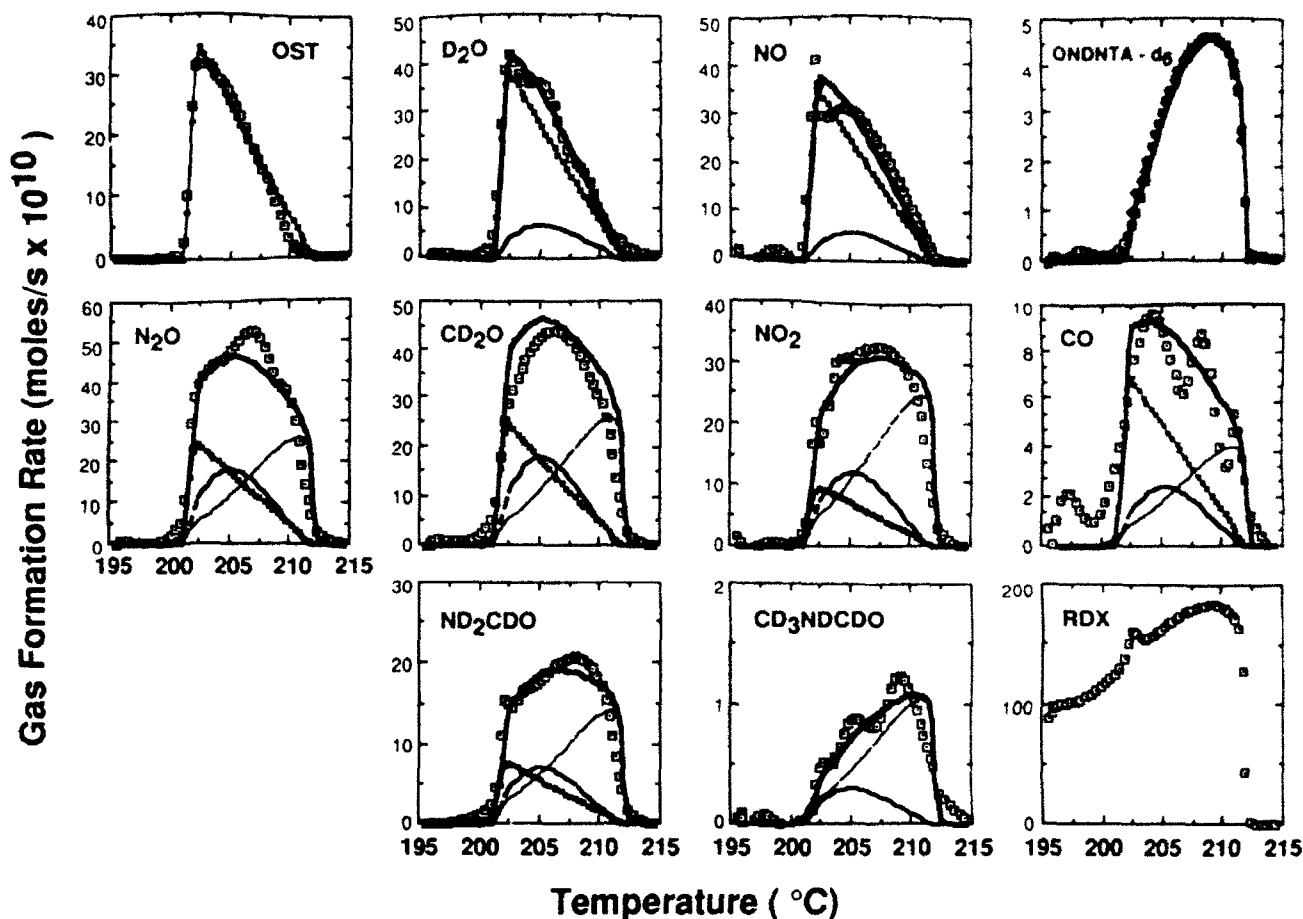


Figure 10. Gas formation rates of the products formed in experiment II with RDX- d_6 along with the fits to the data based on the four primary decomposition pathways. The bold line (—) in all of the graphs represents the total contribution from all of the reaction channels. The square-dot lines for OST, D₂O, and NO represent the contribution by reaction pathway P1. The thin dashed (---) lines shown in N₂O, CD₂O, NO₂, CO, and ND₂CDO represent the contributions from reaction pathway P2. The bold dashed lines (---) represent the contribution from the ONDNTA decomposition pathway P3. The thin solid lines (—) that peak near the highest temperature correspond to the contribution from the catalytic decomposition pathway P4. The fit to the CD₂O data uses same coefficients as used to fit the N₂O data thus assuming that CD₂O and N₂O are formed in equal amounts. The difference between the calculated and measured gas formation rates for CD₂O indicates the amount of CD₂O that reacts prior to leaving the reaction cell.

(experiment I) and Figure 10 for RDX- d_6 (experiment II). From Figures 9 and 10, it can be seen that OST and ONDNTA exhibit relatively simple temporal behaviors and are representative of reaction pathways P1 and P3, respectively, whereas the other products have temporal behaviors that are determined by more than one reaction channel.

OST. The rate of formation of OST and, to a certain extent, the rates of formation of H₂O and NO decrease in direct proportion to the amount of RDX remaining in the reaction cell. This behavior indicates that the decomposition reaction is first order in the amount of RDX and supports a possible unimolecular decomposition mechanism. The rates of formation of H₂O and NO are similar to OST except for the presence of a shoulder on the curve that originates from reaction pathway P3. The calculated rate of formation of OST, shown in Figures 9 and 10, is based on the simple first-order rate expression

$$\frac{dn_{\text{OST}}}{dt} = k_1 n_{\text{RDX}(l)} \quad (1)$$

where n_{OST} is the amount of OST, k_1 is the rate constant, and $n_{\text{RDX}(l)}$ is the amount of liquid RDX present. The amount of liquid RDX present during melting is assumed to be a linear function of time between the onset and completion of melting, and it is determined by optimizing the fit to the data. The fits to the OST data shown in Figures 9 and 10 predict the general trend in the formation of OST quite well. However, the fits overpredict the amount of OST present as the sample is heated, and they also assume that the rate constant is independent of temperature. This behavior indicates that eq 1 does not adequately represent all of the reactions that involve OST. For example, it is quite possible

that OST also decomposes in the reaction cell and eq 1 should contain a term to represent the decomposition of OST. Unfortunately, although the decomposition of OST to HCN is likely, it is not readily apparent from the data what fraction of the HCN originates from the decomposition of OST, and thus, an appropriate expression to account for its decomposition has not been included in the analysis.

ONDNTA. The increasing rate of ONDNTA release from the reaction cell as the quantity of RDX decreases seems contrary to initial expectations. However, since ONDNTA is very similar to RDX, we assume that it will form an ideal solution with RDX. Furthermore, if we assume that its vapor pressure is approximately equal to that of RDX, then we may express its release from the reaction cell as

$$\frac{d(n_{\text{ONDNTA}})_r}{dt} = \frac{dn_{\text{RDX}}}{dt} \frac{n_{\text{ONDNTA}}}{n_{\text{ONDNTA}} + n_{\text{RDX}}} \quad (2)$$

where dn_{RDX}/dt is the rate of release of RDX from the reaction cell and n_{ONDNTA} is the amount of ONDNTA in solution. The amount of ONDNTA present in the reaction cell at any time during the experiment may be expressed as

$$\frac{d(n_{\text{ONDNTA}})_c}{dt} = k_{3f} n_{\text{RDX}} [\text{NO}] - k_{3d} n_{\text{ONDNTA}} - \frac{dn_{\text{RDX}}}{dt} X_{\text{ONDNTA}} \quad (3)$$

where k_{3f} is the pseudo-rate constant for formation of ONDNTA, k_{3d} is the rate constant for decomposition of ONDNTA, [NO] is the concentration of NO in the reaction cell, and X_{ONDNTA} is

the mole fraction of ONDNTA in the liquid. The first term on the right side of eq 3 represents the rate of formation of ONDNTA, and since the isotopic scrambling results (see next paper) indicate that it is formed via reactions R2 and R3, it has been made first order in both RDX and NO. Since the reactions occur within the liquid RDX, the rate of formation of ONDNTA is actually proportional to the amount of NO in the liquid. Therefore, k_{3f} includes a term that relates the amount of NO in the liquid to its concentration in the gas phase in the reaction cell in addition to the rate constant for the reaction. The second term represents the decomposition of ONDNTA. Our preliminary studies of the decomposition of ONDNTA show that its major decomposition products are N_2O and CH_2O . Since specifics of the decomposition mechanism of ONDNTA are presently unknown, it is assumed a priori that the decomposition is first order in ONDNTA. The third term represents the loss of ONDNTA from the reaction cell through the orifice. The constants k_{3f} and k_{3d} are varied to give the best fits to the ONDNTA data shown in Figures 9 and 10.

It is interesting to note that even though the isotopic scrambling experiments²⁴ with pure RDX and RDX- d_6 do not exhibit a DKIE in the formation of ONDNTA, the rate of formation of ONDNTA is significantly higher for unlabeled RDX (Figure 9) than it is for RDX- d_6 (Figure 10). The maximum rate of formation of ONDNTA for unlabeled RDX is 4.5×10^{-5} mol/s per mole of RDX present at the start of the experiment compared to a maximum rate of 1.4×10^{-5} mol/s for RDX- d_6 . This large difference is most likely due to the lower rate of formation of NO from pathway P1, which exhibits a primary DKIE, resulting in the formation of less ONDNTA in the experiment with RDX- d_6 . In contrast, since the isotopic scrambling experiments²⁴ were conducted with solutions of unlabeled RDX and RDX- d_6 , the concentration of NO available for reaction R3 was the same for both the unlabeled RDX and RDX- d_6 , and hence a DKIE was not observed for the formation of ONDNTA. This behavior further illustrates the complexity of the thermal decomposition of RDX, since not only are there several parallel reaction pathways that lead to the products, but the reaction pathways are also coupled.

H_2O , NO . The gas formation rates of water and NO, shown in Figures 9 and 10, also exhibit temporal behaviors that indicate that their rates of formation are first order in RDX. This behavior is consistent with their formation via pathway P1 in which RDX decomposes via reaction R8 to OST and HONO followed by the subsequent reaction of HONO via reaction R7 to form H_2O and NO. The gas formation rates for this reaction pathway are simply expressed as

$$\frac{dn_{H_2O}}{dt} = a_{H_2O} \frac{dn_{OST}}{dt}; \quad \frac{dn_{NO}}{dt} = a_{NO} \frac{dn_{OST}}{dt} \quad (4)$$

where a_{H_2O} and a_{NO} are stoichiometric factors, and the results are shown as the square-dot lines in Figures 9 and 10.

The results for H_2O and NO also indicate that a portion of these products originate from reaction pathway P3. Since the mechanism for the decomposition of ONDNTA is unknown at present, the gas formation rates of the products formed from pathway P3 are simply expressed as

$$\frac{dn_{prod_i}}{dt} = c_i k_{3d} n_{ONDNTA} \quad (5)$$

where $3i$ represents the product formed from reaction pathway P3 and c_i is an empirical constant. The contributions of H_2O and NO formed by reaction pathway P3 to the total gas formation rates of H_2O and NO are shown in Figures 9 and 10. Note that the contribution to the H_2O and NO gas formation rates from pathway P3 is greater for the unlabeled RDX than for RDX- d_6 . As was the case for ONDNTA, this is consistent with reaction pathway P1 exhibiting a DKIE and thus producing less NO that is needed to form ONDNTA via reaction R3. Consequently, RDX- d_6 forms less ONDNTA by pathway P3 which in turn produces less H_2O and NO.

N_2O , CH_2O , NO_2 , HCN , CO , NH_2CHO . The temporal behaviors of the gas formation rates for N_2O , CH_2O , NO_2 , CO ,

HCN , and NH_2CHO are characterized by a rapid increase in these signals when the sample melts, followed by a more gradual increase in the gas formation rates, and a continuation of relatively large gas formation rates near the end of the experiments when the sample is almost entirely depleted. The rapid increase in the gas formation rates as the sample melts is attributed to the unimolecular decomposition of RDX according to the reaction shown as pathway P2. The more gradual increase in these products is attributed to the decomposition of ONDNTA, by reaction pathway P3. However, these two decomposition pathways alone cannot account for the large amounts of these products that are formed at the end of the experiment when little RDX remains. Therefore, three other reaction pathways were considered to explain this behavior. First, gas-phase decomposition of RDX was considered since its vapor pressure within the reaction cell is independent of the amount of pure liquid-phase RDX present in the cell and its decomposition would explain the observed temporal behaviors of these products. However, this pathway was rejected because gas-phase decomposition does not play a significant role in our experiments as discussed above. Also considered was the decomposition of ONDNTA in the gas phase. With this pathway it was not possible to obtain a fit to the data that matched even the general features of their temporal behaviors. The third path considered, and finally used, was a catalytic channel. Since the decomposition of RDX in the reaction cell produced a small amount of brownish residue on the walls of the reaction cell, it was assumed that this coating may catalyze the decomposition of the liquid- or gas-phase RDX as it comes in contact with the walls of the reaction cell. The following simple expression was used to characterize the rate of gas formation of the various products from the catalytic reaction pathway P4

$$\frac{dn_{prod_i}(t)}{dt} = d_i k_4(t) [RDX(t)] \quad (6)$$

where $4i$ represents the product formed from reaction pathway P4, d_i is the stoichiometric factor that relates the number of molecules of product i formed per molecule of RDX decomposed by pathway P4, $k_4(t)$ is the time-dependent rate constant that characterizes both the growth in the amount of catalyst present in the reaction cell and its rate of reaction with RDX, and $[RDX(t)]$ is the concentration of RDX in contact with the catalyst at time t . For the fits to the data shown in Figures 9 and 10, $k_4(t)$ was assumed to have a linear growth rate starting at zero when the sample melted. The value of the growth rate was determined from the best fit to the data. This simple treatment of the catalytic pathway is used since it seems reasonable that the amount of catalyst present in the reaction cell may accumulate as it is formed by reaction of the RDX decomposition products. The reaction between the RDX and the catalyst may very well not be characterized by the linear rate assumed here, but there is not sufficient evidence to warrant any more sophisticated treatment. The main point of invoking the catalytic channel is that this type of behavior is able to account for the formation of the N_2O , CH_2O , NO_2 , CO , HCN , and NH_2CHO products during the later stages of the decomposition. Reaction pathway P4 is the least well-defined, and further studies would be required to determine more details. The fits to the data using reaction pathways P2–P4 are shown in Figures 9 and 10.

It is interesting to note that, unlike HMX² in which it was postulated that H_2O may act as a catalyst in its solid-phase decomposition, water does not appear to catalyze the decomposition of RDX in the liquid phase. If water catalyzes the decomposition of liquid-phase RDX, then one would expect the rate of gas formation of the products formed from this channel to be dependent on the amount of water present in the reaction cell. From the data in Figures 9 and 10, it is clear that the water present in the reaction cell decreases as the experiment progresses and one would expect a decreasing amount of products formed via the catalytic pathway if water was the catalyst. However, this does not rule out the possibility that water acts as a catalyst of HMX because in the solid phase the concentration of the water in contact with HMX will be much higher than in the liquid-phase RDX since it is trapped within the HMX particles.

TABLE IV: Fraction of RDX Decomposed by Each Reaction Pathway

pathway	reaction	fraction of decomposed (%)	
		RDX	RDX- d_6
P1	unimolecular RDX \rightarrow OST	30	33
P2	unimolecular RDX N-NO ₂ bond breaking	10	14
P3	RDX \rightarrow ONDNTA \rightarrow products	35	25
P4	catalysis of RDX	25	28

CH₃NHCHO. The gas formation rate of CH₃NHCHO gradually grows during the experiment and peaks as the sample nears complete depletion in a manner similar to ONDNTA. This behavior may arise from either the decomposition of a polyamide that is formed during the decomposition or from an increasing concentration of the amide in the solution in the reaction cell. Since the vapor pressure of *N*-methylformamide (NMFA) is relatively high, this suggests that little NMFA will remain in solution. However, the results from the TOF velocity spectra measurements indicate that the molecular weight of the species that evolves from the reaction cell and produces the ion signals associated with the NMFA product has a molecular weight that is approximately twice that of NMFA, suggesting that NMFA is present in the form of a dimer. The vapor pressure of this species may be sufficiently low that its release rate may be determined by its mole fraction in the solution. Since neither of these sources of NMFA can be ruled out, it is not possible to determine whether NMFA originates from reaction R9 or the decomposition of the polyamide that leads to the formation of the residue.

The relative amounts of RDX that decompose by each of these different reaction pathways, as estimated from the fits to the data shown in Figures 9 and 10 using the simple model, are given in Table IV. These results illustrate that the lower molecular weight products formed during the thermal decomposition of RDX originate from four different primary reaction channels. The reaction channels involving unimolecular decomposition of RDX appear to account for only 40% of the total amount of RDX that decomposes. The other 60% decomposes either through the ONDNTA intermediate or by the catalytic decomposition of RDX.

Comparison with Other Earlier Work. The results of this study are consistent with previous TGA³² and DSC³³ measurements that have shown, through the use of DKIE studies with RDX, that hydrogen is involved in the rate-limiting step. However, due to the limited amount of information obtained in TGA and DSC experiments, these studies were unable to identify the products associated with the rate-limiting step, the presence of concurrent decomposition pathways that do not involve hydrogen in the rate-limiting step, nor where the rate-limiting step occurs in the reaction pathway. The first-order reaction behavior observed in the DSC experiments is consistent with reaction pathway P1 observed in the present study. Unfortunately, the DSC and TGA experiments cannot account for a concurrent reaction pathway P2 that does not exhibit a DKIE since the extent of the DKIE for a given reaction is dependent on several different parameters. Furthermore, the very subtle manner in which the DKIE manifests itself in reaction pathway P3 is not typically considered in interpretation of results from DKIE experiments. In the case of pathway P3, the DKIE expresses itself by limiting the amount of ONDNTA that is formed by controlling the amount of NO that is produced by reaction channel P1. As discussed in the following paper, neither the formation of ONDNTA nor its decomposition to CH₂O and N₂O exhibit a DKIE. Consequently, reaction pathway P3, which produces a large fraction of the CH₂O and N₂O in thermal decomposition experiments with RDX, is overlooked in interpreting the DKIE results from conventional DSC and TGA experiments.

A comparison of the decomposition of RDX with that of dimethylnitramine (DMNA) illuminates the contrasting features of their decomposition reactions. The studies with DMNA²⁰⁻²² have found that the major product formed in the decomposition

of DMNA is *N,N*-dimethylnitrosamine (DMNO) [(CH₃)₂N-N-O]. The studies by Fluornoy²⁰ and Lin²¹ explained this product by the reaction of NO with the dimethylamino radical whereas Nigenda et al.²² invoked additional channels including nitro-nitrate rearrangement and displacement of the nitrite by NO to explain their results. Melius and Binkley²⁴ on the other hand suggest that radical addition to one of the nitro group oxygens leads to the formation of DMNO. In our experiments the reaction of NO with the amino radical left after the N-NO₂ bond scission to form ONDNTA is similar to the decomposition of DMNA and is consistent with the complete isotopic scrambling of the N-NO nitrogens observed (see next paper) in the ONDNTA product. The isotopic scrambling also precludes the formation of ONDNTA via radical addition to one of the nitro group oxygens followed by the direct abstraction of the oxygen atom. Since reaction pathway P1 produces NO during the decomposition of RDX, the source of NO that participates in the recombination reaction with the amino radical is not in question as it is for the formation of DMNO from DMNA.²²

Further comparison of the decomposition of RDX with that of DMNA shows that the primary first-order reaction pathway for RDX that produces OST and exhibits a DKIE does not have an analogous pathway in the decomposition of DMNA. Consequently, although the study of the simpler DMNA molecule provides insight into certain aspects of nitramine decomposition that are applicable to the more complicated RDX molecule, our results on RDX show that DMNA does not mimic all of the reaction pathways that occur during the decomposition of RDX and that it is necessary to study RDX itself to fully understand its decomposition.

Comparison of our results on the thermal decomposition of RDX in the bulk with the results from the unimolecular IRMPD of RDX under collision-free conditions in a molecular beam provides intriguing contrasts and raises the question of how molecules that surround a decomposing RDX molecule affect its decomposition. The most dramatic difference between these two types of experiments is the decomposition of approximately 30% of the RDX (70-75% of the RDX whose decomposition is solely first order in RDX) in the liquid phase via pathway P1 to form OST and the apparent absence of this decomposition pathway in the IRMPD experiments. This difference could readily be explained by the occurrence of secondary reactions between the decomposition RDX and its decomposition products if it were not for several important aspects of its formation. First, the rate of formation of OST is first order in RDX and independent of the concentration of any other species. Second, as discussed in the following paper, OST does not undergo isotopic scrambling of any of its elements (i.e., all of the atoms in one OST molecule originate from one RDX molecule). These results imply that the ring from the RDX molecule remains intact and the oxygen atom and three hydrogen atoms on the ring all remain from the original molecule. The ion representing OST ($m/z = 97$) was not reported in the IRMPD results. Possible explanations for this discrepancy are (1) the reaction "temperatures" in the IRMPD experiments are between 200 and 300 °C higher than the thermal decomposition temperatures used in our experiments thus precluding this channel in the IRMPD experiments; (2) the analysis of the IRMPD data may not have considered the formation of OST by reaction R8 which is somewhat similar to reactions A and II in ref 23; or (3) the close proximity of adjacent RDX molecules in the liquid phase may alter the unimolecular decomposition mechanism due to effects such as hydrogen bonding. At this time it is not clear which of these three explanations are more likely.

Another difference between our results and those from the IRMPD experiments is the large fraction (0.67) of RDX that decomposed through the concerted symmetric triple fission (CSTF) to form three methylenenitramine fragments that subsequently decomposed in secondary reactions to HCN, HONO, N₂O, and CH₂O in the IRMPD experiments. In our thermal decomposition experiments only about 10% of the RDX that decomposes (25% of the RDX whose decomposition is solely first order in RDX) produces products (N₂O and CH₂O) that may

be formed through the CSTF mechanism. The CSTF mechanism may be responsible for this 10% of the RDX that decomposes. However, our results are also consistent with reaction



followed by the decomposition of the two methylenimine fragments. H_2CN is a species that is likely to form the NMFA observed in the decomposition. The NO_2 that originates from unimolecular RDX decomposition may be formed by either pathways P1 or P2. Thus it is not clear whether N- NO_2 bond breaking or the CSTF mechanism leads to the N_2O and CH_2O products formed in reaction pathway P2.

It is clear from the results that neither experiments with simpler nitramines such as DMNA nor elegant unimolecular decomposition experiments fully address the reaction mechanisms that control the decomposition of RDX in the solid and liquid phases. It is evident that the formation of ONDNTA and its subsequent decomposition to final products and the catalytic decomposition of RDX both play important roles in determining the identities and rates of formation of the products from the thermal decomposition of RDX. Controlling these decomposition pathways through the use of additives or the synthesis of nitramines with slightly different molecular configurations may provide avenues for developing propellants with better combustive properties.

From our results showing the presence of four primary pathways that control the thermal decomposition of RDX in the liquid phase, it is readily apparent why there have been so many conflicting results on both the identities of its decomposition products and its rate of decomposition. When this is combined with the different decomposition behavior observed in the solid phase, the interpretation of the results from experiments that either identify reaction intermediates, measure the distribution of final products, or measure thermochemical behaviors, in terms of various simple bond-breaking sequences, provides an inadequate framework for understanding the very complex mechanisms that control the decomposition of RDX and HMX. The changing nature of the sample of RDX, due to its interaction with its decomposition products during the course of an experiment, makes variation of the experimental results very likely and dependent on the exact conditions used for each individual experiment.

Conclusions

Through the use of STMBMS measurements, TOF velocity-spectra analysis, and ^2H , ^{13}C , ^{15}N , and ^{18}O labeled analogues of RDX, the thermal decomposition products of RDX have been identified as H_2O , HCN , CO , CH_2O , NO , N_2O , NH_2CHO , NO_2 , HONO , $(\text{CH}_2)_2\text{NHCHO}$, *oxy-s*-triazine, and ONDNTA. By measuring the temporal behaviors of the gas formation rates of each of these products during the course of a decomposition experiment, the existence of four primary reaction pathways that control the decomposition of RDX in the condensed phase have been discovered.

In the liquid phase, four primary reaction pathways control the decomposition of RDX. These reaction pathways consist of two pathways that are first-order reactions solely in RDX, suggesting that these are unimolecular decomposition routes. Of these two pathways, one produces predominantly OST , NO , and H_2O and accounts for approximately 30% of the decomposed RDX, and the other produces predominantly N_2O and CH_2O with smaller amounts of NO_2 , CO , and NH_2CHO and accounts for 10% of the decomposed RDX. The third pathway consists of formation of ONDNTA by reaction between NO , produced in the first decomposition pathway, with the amino radical, produced after scission of the N- NO_2 bond in RDX and the subsequent decomposition of ONDNTA to predominantly CH_2O and N_2O . The fourth reaction pathway consists of decomposition of RDX through reaction with a catalyst that is formed from the decomposition products of previously decomposed RDX. The third and fourth reaction channels each account for approximately 30% of the decomposed RDX.

The formation of N_2O and CH_2O via the other unimolecular decomposition channel is consistent with both N- NO_2 bond

breaking followed by the subsequent decomposition of the remaining fragment of N_2O and CH_2O , possibly via the $\text{CH}_2=\text{N}-\text{NO}_2$ intermediate and also via the concerted symmetric triple fission of RDX to three $\text{CH}_2=\text{N}-\text{NO}_2$ fragments, and their subsequent decomposition to N_2O and CH_2O . However, the formation of CH_2NHCHO may possibly originate by reaction of CH_2O with the H_2CN radical left from the unraveling of the RDX ring after the breaking of the N- NO_2 bond, thus indicating that the N- NO_2 bond breaking channel may be the more likely explanation for this reaction channel.

Our experiments with solid-phase RDX have shown that its decomposition rate is much slower than that of liquid-phase RDX. ONDNTA is the only product that appears to be formed during the early stages of its decomposition. As the decomposition of solid RDX continues, N_2O and smaller amounts of CH_2O start to evolve from the sample. After the evolution rate of these two products increases, the products associated with the liquid-phase RDX decomposition appear and their rate of gas formation rapidly increases. This strongly suggests that the decomposition of solid RDX occurs through formation of ONDNTA within the lattice, the subsequent decomposition of ONDNTA within the lattice to N_2O and CH_2O , followed by the dispersion of CH_2O in the RDX leading to its eventual liquefaction, and the onset of the liquid-phase decomposition reactions.

The complexity of the decomposition pathways that control the identities of the decomposition products and their rates of formation and the changing nature of the decomposing sample itself illustrate the necessity of correlating the identities and rates of formation of the various products with the composition of the sample at any given time during its decomposition. If this is not done, the products that are detected cannot be correlated with the individual reaction pathways, thus making the interpretation of their appearance ambiguous.

Acknowledgment. The authors thank M. G. Mitchell and K. A. Morrison for assistance in running the experiments and collecting the data, C. Schaeffer for assistance in developing the procedure for analyzing the TOF data, and J. R. Autera for assistance in the isotopic syntheses. This research was supported in part by the U.S. Army Research Office, a joint Memorandum of Understanding between the U.S. DOE and the U.S. Army, and the U.S. Army ARDEC.

References and Notes

- (1) Behrens, R., Jr. *J. Phys. Chem.* **1990**, *94*, 6706.
- (2) Behrens, R., Jr.; Bulusu, S. *J. Phys. Chem.* **1991**, *95*, 5838.
- (3) (a) Schroeder, Michael A. Critical Analysis of Nitramine Decomposition Data: Product Distributions from HMX and RDX. U.S. Army Ballistic Research Laboratory Report BRL-TR-2659, 1985. (b) Schroeder, Michael A. Critical Analysis of Nitramine Decomposition Data: Activation Energies and Frequency Factors for HMX and RDX Decomposition. U.S. Army Ballistic Research Laboratory Report BRL-TR-2673, 1985.
- (4) Boggs, T. L. The Thermal Decomposition Behavior of Cyclotriethylene-trinitramine (RDX) and Cyclotetramethylene-tetranitramine (HMX). In *Fundamental of Solid-Propellant Combustion*; Kuo, K. K., Summerfield, M., Eds.; Progress in Astronautics and Aeronautics Vol. 90; AIAA Inc.: New York, 1984; p 121.
- (5) Fifer, R. A. Chemistry of Nitrate Ester and Nitramine Propellants. In *Fundamentals of Solid-Propellant Combustion*; Kuo, K. K., Summerfield, M., Eds.; Progress in Astronautics and Aeronautics Vol. 90; AIAA Inc.: New York, 1984; p 177.
- (6) Robertson, A. J. *B. Trans. Faraday Soc.* **1949**, *45*, 85.
- (7) Rauch, F. C.; Fanelli, A. J. *J. Phys. Chem.* **1969**, *73*, 1604.
- (8) Cosgrove, J. D.; Owen, A. J. *Combust. Flame* **1974**, *22*, 13.
- (9) (a) Batten, J. J.; Murdie, D. C. *Aust. J. Chem.* **1970**, *23*, 737. (b) Batten, J. J.; Murdie, D. C. *Aust. J. Chem.* **1970**, *23*, 749. (c) Batten, J. J. *Aust. J. Chem.* **1971**, *24*, 945. (d) Batten, J. J. *Aust. J. Chem.* **1971**, *24*, 2025. (e) Batten, J. J. *Aust. J. Chem.* **1972**, *25*, 2337.
- (10) Cosgrove, J. D.; Owen, A. J. *Combust. Flame* **1974**, *22*, 19.
- (11) Goshgarian, B. B. Air Force Rocket Propulsion Laboratory Report, AFRPL-TR-78-76, 1976.
- (12) Farber, M.; Srivastava, R. D. *Chem. Phys. Lett.* **1979**, *64*, 307.
- (13) Stals, J. *Trans. Faraday Soc.* **1971**, *67*, 1768.
- (14) Bulusu, S.; Graybush, R. J. Proceedings of the 36th International Congress on Industrial Chemistry, Brussels, Belgium, 1967. *C. R. Ind. Chim. Belge* **1967**, *32*, 1.
- (15) Suryanarayana, B.; Graybush, R. J.; Autera, J. R. *Chem. Ind. (London)* **1967**, 2177.
- (16) (a) Axworthy, A. E.; Flanagan, J. E.; Woolery, D. O. *Proceedings of the 15th JANNAF Combustion Meeting*; CPIA Publication No. 297,

Chemical Propulsion Information Agency: Laurel, MD, 1978; Vol. 1, p 253.
 (b) Axworthy, A. E.; Flanagan, J. E.; Woolery, D. O.; Gray, J. C. CPIA Publ. No. 308, *Proceedings of the 16th JANNAF Combustion Meeting*; CPIA Publication No. 308; Chemical Propulsion Information Agency: Laurel, MD, 1979; Vol. III, 289.
 (17) Oyumi, Y.; Brill, T. B. *Combust. Flame* **1985**, *62*, 213.
 (18) Hoffsommer, J. C.; Glover, D. J.; Elban, W. L. *J. Energ. Mater.* **1985**, *J.* 149.
 (19) Sharma, J.; Hoffsommer, J. C.; Glover, D. J.; Coffey, C. S.; Forbes, J. W.; Liddiard, T. P.; Elban, W. L.; Santiago, F. *Proceedings of the Eighth Symposium (International) on Detonation*, Albuquerque, NM, 1985; Government Printing Office: Washington, DC, 1985; p 725.
 (20) Fluornoy, J. M. *J. Chem. Phys.* **1962**, *36*, 1106.
 (21) Lloyd, S. A.; Unstead, M. E.; Lin, M. C. *J. Energ. Mater.* **1985**, *J.* 187.
 (22) Nigenda, S. E.; McMillen, D. F.; Golden, D. M. *J. Phys. Chem.* **1989**, *93*, 1124.
 (23) Zhao, X.; Hintsä, E. J.; Lee, Y. T. *J. Chem. Phys.* **1988**, *88*, 801.
 (24) Behrens, R., Jr.; Bulusu, S. *J. Phys. Chem.*, following paper in this issue.
 (25) (a) Behrens, R., Jr. *Rev. Sci. Instrum.* **1986**, *58*, 451. (b) Behrens, R., Jr. The Application of Simultaneous Thermogravimetric Modulated Beam Mass Spectrometry and Time-of-Flight Velocity Spectra Measurements to

the Study of the Pyrolysis of Energetic Materials. In *Chemistry and Physics of Energetic Materials*; Bulusu, S. N., Ed.; *Proceedings of the NATO Advanced Study Institute*, Vol. 309; Kluwer Academic Publishers: Dordrecht, The Netherlands, 1990; p 327.
 (26) Behrens, R., Jr. *Int. J. Chem. Kinet* **1990**, *22*, 135.
 (27) Behrens, R., Jr. *Int. J. Chem. Kinet* **1990**, *22*, 159.
 (28) Behrens, R., Jr. *Proceedings of the 23rd JANNAF Combustion Meeting*, Langley, VA; CPIA Publication No. 457; Chemical Propulsion Information Agency: Laurel, MD, 1986; pp 231-240.
 (29) Snyder, A. P.; Kremer, J. H.; Liebman, S. A.; Schroeder, M. A.; Fifer, R. A. *Org. Mass Spectrom.* **1989**, *24*, 15.
 (30) Maksimov, Y. Y.; Apal'kova, V. N.; Braverman, O. V.; Solov'ev, A. I. *Russ. J. Phys. Chem.* **1985**, *59*, 201.
 (31) (a) Pollard, F. H.; Wyatt, R. M. H. *Trans. Faraday Soc.* **1949**, *49*, 760. (b) He, Y.; Kolby, E.; Shumaker, P.; Lin, M. C. *Int. J. Chem. Kinet* **1989**, *21*, 1015.
 (32) Bulusu, S.; Weinstein, D. I.; Autera, J. R.; Velicky, R. W. *J. Chem.* **1986**, *90*, 4121.
 (33) Rodgers, S. L.; Coolidge, M. B.; Lauderdale, W. J.; Shackelford, S. A. *Thermochim. Acta* **1991**, *177*, 151.
 (34) Melius, C. F.; Binkley, J. S. In *Proceedings of the 21st Symposium (International) on Combustion*, 1987; The Combustion Institute: Pittsburgh, PA, 1988; p 1953.

DISTRIBUTION LIST

Commander
Armament Research, Development and Engineering Center
U.S. Army Armament, Munitions and Chemical Command
ATTN: SMCAR-IMI-I (3)
SMCAR-AEE (3)
SMCAR-AEE-B (5)
Picatinny Arsenal, NJ 07806-5000

Commander
U.S. Army Armament, Munitions and Chemical Command
ATTN: AMSMC-GCL (D)
Picatinny Arsenal, NJ 07806-5000

Administrator
Defense Technical Information Center
ATTN: Accessions Division (12)
Cameron Station
Alexandria, VA 22304-6145

Director
U.S. Army Material Systems Analysis Activity
ATTN: AMXSY-MP
Aberdeen Proving Ground, MD 21005-5066

Commander
Chemical Research, Development and Engineering Center
U.S. Army Armament, Munitions and Chemical Command
ATTN: SMCCR-MSI
Aberdeen Proving Ground, MD 21010-5423

Director
U.S. Army Edgewood Research, Development and Engineering Center
ATTN: SCBRD-RTT (Aerodynamics Technical Team)
Aberdeen Proving Ground, MD 21010-5423

Director
Ballistic Research Laboratory
ATTN: AMXBR-OD-ST
Aberdeen Proving Ground, MD 21005-5066

Chief
Benet Weapons Laboratory, CCAC
Armament Research, Development and Engineering Center
U.S. Army Armament, Munitions and Chemical Command
ATTN: SMCAR-CCB-TL
Watervliet, NY 12189-5000

Commander
U.S. Army Rock Island Arsenal
ATTN: SMCAR-TL, Technical Library
Rock Island, IL 61299-5000

Director
U.S. Army TRADOC Systems Analysis Activity
ATTN: ATAA-SL
White Sands Missile Range, NM 88002